Constraining anomalous Higgs boson couplings to the heavy-flavor fermions using matrix element techniques

Andrei V. Gritsan,[1,*] Raoul Röntsch,[2,†] Markus Schulze,[3,‡] and Meng Xiao[1,§]

[1]*Department of Physics and Astronomy, Johns Hopkins University, Baltimore, Maryland, USA*
[2]*Karlsruhe Institute of Technology, Karlsruhe, Germany*
[3]*CERN, European Organization for Nuclear Research, Geneva, Switzerland*

(Received 7 June 2016; published 19 September 2016)

In this paper, we investigate anomalous interactions of the Higgs boson with heavy fermions, employing shapes of kinematic distributions. We study the processes $pp \to t\bar{t} + H$, $b\bar{b} + H$, $tq + H$, and $pp \to H \to \tau^+\tau^-$ and present applications of event generation, reweighting techniques for fast simulation of anomalous couplings, as well as matrix element techniques for optimal sensitivity. We extend the matrix element likelihood approach (MELA) technique, which proved to be a powerful matrix element tool for Higgs boson discovery and characterization during Run I of the LHC, and implement all analysis tools in the JHU generator framework. A next-to-leading-order QCD description of the $pp \to t\bar{t} + H$ process allows us to investigate the performance of the MELA in the presence of extra radiation. Finally, projections for LHC measurements through the end of Run III are presented.

DOI: 10.1103/PhysRevD.94.055023

I. INTRODUCTION

The discovery [1,2] of the H boson by the ATLAS and CMS experiments during Run I of the LHC marked an important milestone in the evolution of our understanding of fundamental particle physics. One of the most important goals now is a precise understanding of the newly discovered state, including its couplings to other particles as well as its CP nature. Any significant deviation from Standard Model (SM) predictions would reveal the existence of new physics in the Higgs sector and should to be classified according to its anomalous coupling structures. Likewise, in the case of a discovery of a new resonance at the LHC, a similar program of investigating properties and couplings is required.

Since experimental efforts during Run I mostly focused on the H boson decaying to a pair of vector bosons,[1] extensive studies of the HVV couplings and corresponding CP properties were performed [3–6], leading to results consistent with the Standard Model nature of the H boson with quantum numbers $J^{PC} = 0^{++}$. However, many generic models of new physics predict deviations which are beyond the current experimental precision [7]. This leaves ample room for anomalous interactions to hide as small modifications of the SM structure. Moreover, a complete knowledge of the SM Higgs mechanism requires the study of the H boson interactions with fermions. While the observation of Hgg and $H\gamma\gamma$ interactions established the $Ht\bar{t}$ coupling through a closed loop, a detailed understanding only arises from the observation of various mass hierarchies, as well as the minimal flavor-universal Yukawa interaction as predicted by the SM. Hence, it is of paramount importance to investigate possible anomalous coupling patterns with which different quarks and leptons may interact with the Higgs field. The most promising approach is the study of differential distributions in processes with *direct* sensitivity through the associated production of the H boson with on-shell fermions, $f'\bar{f} + H$, or through the decay $H \to f\bar{f}$.

There has been considerable effort in modeling the $Hf\bar{f}$ couplings and developing tools for their analysis in associated production [8–31] and in the $H \to \tau^+\tau^-$ decay [32–38]. Current experimental analyses have measured the coupling strength of $Hb\bar{b}$ and $Ht\bar{t}$ only through closed loops [4,6]. There have been experimental searches for the H boson production in association with a single top quark [39] and with $t\bar{t}$ [40–43], with strong evidence for the latter in Run I of the LHC. The process $b\bar{b}H$ has not been studied with a dedicated analysis so far, but there is evidence for the H boson decay into $b\bar{b}$ pairs [44–46]. The decay of $H \to \tau^+\tau^-$ is observed when results of CMS [47] and ATLAS [48] are combined, and searches in this decay channel have been performed for specific scenarios beyond the SM [49–51]. However, an interpretation in terms of generic anomalous couplings has not yet been undertaken.

All these measurements require sophisticated tools for the optimal extraction of statistical information, as data

*gritsan@pha.jhu.edu
†raoul.roentsch@kit.edu
‡markus.schulze@cern.ch
§mxiao3@jhu.edu

[1]In this paper, HVV couplings induced by closed fermionic loops are still considered to be couplings to vector bosons.

remain limited for detailed analyses of the fermion couplings. The matrix element approach is one such technique, which has been proven successful in setting constraints on HVV couplings using Run I data from CMS [2,3,19,52–58] and ATLAS [5,59,60]. In this paper, we focus on applications to Run II of the LHC and extend our earlier developed techniques for HVV coupling measurements [61–63] to $Hf\bar{f}$ couplings in $t\bar{t}H$, $b\bar{b}H$, and tqH production,[2] as well as to $H \to \tau^+\tau^-$ decays. These matrix element techniques allow the optimal analysis of the dynamics in the production and decay processes. Such techniques have been proposed to enhance signal over background in application to $t\bar{t}H$ production [41,64,65], and we employ them to probe anomalous $Hf\bar{f}$ couplings for the first time. We define the complete set of kinematic observables and the minimal set of matrix-element-based observables necessary to perform the measurements. Moreover, using a next-to-leading-order (NLO) QCD simulation of the $t\bar{t}H$ process that includes a fully consistent treatment of production and decays at higher orders, we demonstrate the robustness of the matrix element approach with respect to additional radiation and loop corrections.

This paper expands our efforts within the broader framework of the JHU generator (JHUGen) and matrix element likelihood approach (MELA) frameworks [61–63]. The rest of the paper is organized as follows. In Sec. II, the formalism of anomalous H boson couplings is discussed. Monte Carlo (MC) simulation with the JHU generator is introduced in Sec. III. The matrix elements technique and the MELA framework are discussed in Sec. IV. A study of NLO QCD effects is presented in Sec. V. In Sec. VI, we discuss the application of these techniques to LHC measurements and make projections to the end of Run III of the LHC. Results are summarized in Sec. VII.

II. PARAMETRIZATION OF HIGGS BOSON COUPLINGS

We describe the interactions between a spin-zero particle H and two fermions through the amplitude

$$\mathcal{A}(Hf\bar{f}) = -\frac{m_f}{v}\bar{\psi}_f(\kappa_f + i\tilde{\kappa}_f\gamma_5)\psi_f, \tag{1}$$

where $\bar{\psi}_f$ and ψ_f are the Dirac spinors, m_f is the fermion mass, and v is the SM Higgs field vacuum expectation value. In the SM, the couplings[3] have the values $\kappa_f = 1$ and $\tilde{\kappa}_f = 0$. Any deviation from these values indicates the presence of physics beyond the SM, which may for example arise through heavy loop-induced fields. In particular, the $\tilde{\kappa}_f$ coupling parametrizes the contribution of a CP-odd pseudoscalar boson, and CP violation occurs when both κ_f and $\tilde{\kappa}_f$ are nonzero.

One may equivalently choose to express the couplings through a Lagrangian (up to an unphysical global phase),

$$\mathcal{L}(Hf\bar{f}) = -\frac{m_f}{v}\bar{\psi}_f(\kappa_f + i\tilde{\kappa}_f\gamma_5)\psi_f H, \tag{2}$$

which allows a connection to be made between the couplings κ_f and $\tilde{\kappa}_f$ and anomalous operators in an effective field theory. We assume the couplings to be independent of kinematics, which corresponds to dimension-6 operators in the effective field theory. Higher-dimension operators could easily be considered through q^2-dependent couplings in our framework, where q is the momentum transfer. However, in our study, we neglect these higher-dimension contributions because they are expected to be small. The hermiticity of the Lagrangian requires κ_f and $\tilde{\kappa}_f$ to be real. Nevertheless, in order to consider the broadest range of scenarios, we allow κ_f and $\tilde{\kappa}_f$ to be complex and trust that, should the unitarity of scattering amplitudes be violated as a result, it will be restored in the full theory. It is convenient to parametrize anomalous couplings through a mixing angle, with $\kappa_f \propto \cos\alpha$ and $\tilde{\kappa}_f \propto \sin\alpha$. Equivalently, we introduce the fractions

$$f_{CP} = \frac{|\tilde{\kappa}_f|^2}{|\kappa_f|^2 + |\tilde{\kappa}_f|^2}, \qquad \phi_{CP} = \arg(\tilde{\kappa}_f/\kappa_f), \tag{3}$$

where the f_{CP} parameter is conveniently bounded between 0 and 1, is uniquely defined, and can be interpreted as the cross section fraction corresponding to the pseudoscalar coupling, and therefore is directly related to experimentally observable effects. It is a convenient counterpart of the f_{a3} parameter defined for the HVV couplings [3,5,63]. While the phase ϕ_{CP} can in general take any value between 0 and 2π, it is reasonable to assume that the ratio $\tilde{\kappa}_f/\kappa_f$ is real; that is, $\phi_{CP} = 0$ or π. However, we do not need to impose this restriction and will also consider other values of ϕ_{CP}. The parameters f_{CP} and ϕ_{CP} in principle depend on the fermion couplings under consideration and should be denoted $f_{CP}^{Hf\bar{f}}$ and $\phi_{CP}^{Hf\bar{f}}$, but in most cases, this will be clear from the context.

The tqH production also involves the HWW coupling. We therefore recall the coupling of the H to two vector bosons [63],[4]

$$\mathcal{A}(HVV) = \frac{1}{v}(a_1 m_V^2 \epsilon_1^* \epsilon_2^* + a_2 f_{\mu\nu}^{*(1)} f^{*(2),\mu\nu} + a_3 f_{\mu\nu}^{*(1)} \tilde{f}^{*(2),\mu\nu}), \tag{4}$$

[2]Unless otherwise noted, tqH refers to all combinations of $t\bar{q}H$, $\bar{t}qH$, tqH, and $\bar{t}\,\bar{q}\,H$ with a quark $q \neq t$.

[3]The coupling convention of Ref. [61] corresponds to $\kappa_f = -\rho_1$ and $\tilde{\kappa}_f = i\rho_2$.

[4]The coupling convention of Ref. [63] corresponds to $a_1 = g_1$, $a_3 = g_2$, and $a_3 = g_4$.

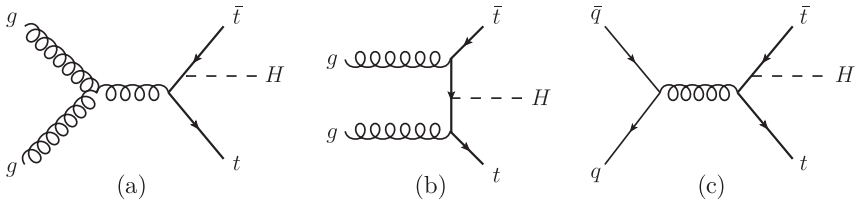

FIG. 1. Representative Feynman diagrams for $t\bar{t}H$ production at leading order.

where ϵ_i is the polarization of the vector boson of mass m_V and momentum q_i, the field strength tensor is $f^{(i),\mu\nu} = \epsilon_i^\mu q_i^\nu - \epsilon_i^\nu q_i^\mu$ and its dual $\tilde{f}^{(i),\mu\nu} = 1/2\epsilon^{\mu\nu\rho\sigma} f^{(i)}_{\rho\sigma}$.

III. MONTE CARLO SIMULATION

The JHU generator framework [61–63] involves both the Monte Carlo generation of unweighted events and the MELA package used in the analysis of the H boson couplings. For top-quark pair production in association with a spin-zero boson H, we compute the leading-order processes $gg \to t\bar{t} + H$ and $q\bar{q} \to t\bar{t} + H$, followed by spin-correlated top-quark decays $t \to bW(\to f'\bar{f})$ in the narrow-width approximation. Any leptonic or hadronic decay mode of the top quarks can be described. Representative Feynman diagrams are shown in Fig. 1, where we allow for the anomalous $Ht\bar{t}$ couplings shown in Eq. (1). The H boson is considered stable in the respective matrix elements describing production, and its decay into any possible channel can be introduced subsequently through processing the generated events using the JHU generator framework.

Since hadronic production of $t\bar{t} + H$ final states involves color flow in initial and final states, additional jet radiation plays an important role in the description of this process. In fact, almost 40% of all $t\bar{t}$ events are accompanied by jets with transverse momentum harder than 40 GeV [66]. It is therefore important to study the impact of radiative corrections on event kinematics and the matrix element observables. To this end, we also calculate the next-to-leading order QCD correction to the $pp \to t\bar{t} + H$ process.

The framework for NLO QCD computations is an extension of the TOPAZ code which two of us developed for anomalous coupling studies of $t\bar{t} + Z$ final states [67,68]. We calculate the virtual correction to the gg and $q\bar{q}$ initial states using the numerical implementation of D-dimensional generalized unitarity techniques [69–72]. The real emission corrections involve the partonic processes $gg \to t\bar{t}g$, $q\bar{q} \to t\bar{t}g$, $qg \to t\bar{t}q$, and $\bar{q}g \to t\bar{t}\,\bar{q}$, which we regularize using the massive dipole subtraction techniques of Refs. [73,74]. A consistent expansion in the strong coupling constant also requires the computation of the NLO corrections to the top-quark decay $t \to bW$ and the subsequent $W \to jj$ decay. We account for these contributions in the narrow-width approximation using the implementation developed in Ref. [75]. Nonresonant and off-shell effects are expected to scale parametrically as $\Gamma_t/m_t \approx 1\%$ and hence can be safely neglected provided that phase space cuts do not severely constrain the top-quark invariant mass. This has been explicitly confirmed in studies for $t\bar{t} + H$ production at leading order (LO) [76] and NLO QCD [77].

We obtain the $pp \to b\bar{b} + H$ process from $pp \to t\bar{t} + H$ by replacing $m_t \to m_b$ in the matrix elements and phase space (and removing the top-quark decay), while preserving the five flavor scheme with massless initial-state quarks. Hence, we neglect the newly appearing t-channel diagram in $bb \to bb$ reactions which is, however, doubly suppressed by the small b-quark parton luminosity. In this way, the H boson is always emitted from the massive final-state quarks only. We believe these approximations are sufficient for studying anomalous interactions in our analysis.

Simulation of the single top-quark production process in association with a spin-zero boson relies on the partonic processes $qb \to q't + H$ (t-channel process) and $q\bar{q}' \to t\bar{b} + H$ (s-channel process). The former topology is shown in Figs. 2(a) and 2(b), and the latter topology is shown in Figs. 2(c) and 2(d). We make use of analytic expressions for the leading-order SM matrix elements [78] and extend them to include anomalous couplings, keeping the five flavor scheme so that the H boson is never radiated off the initial-state b quark. An extensive comparison of the four and five

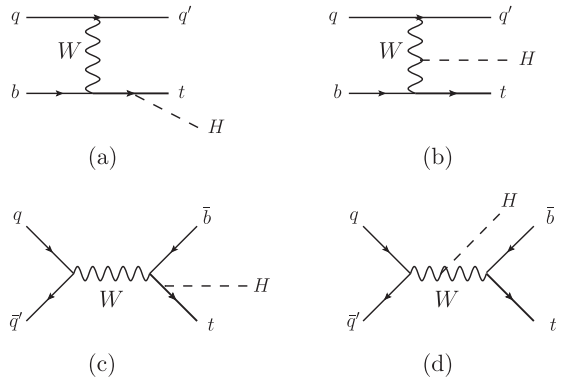

FIG. 2. Feynman diagrams describing the single-top production in association with the H boson. The t-channel process is shown with the H emitted either from the top quark (a) or from the W boson (b); analogous diagrams in the s-channel are shown in (c) and (d).

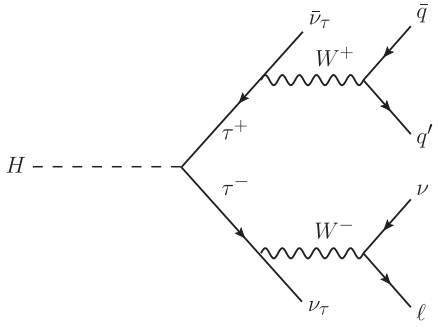

FIG. 3. Feynman diagram describing the decay $H \to \tau\tau$, with one τ subsequently decaying leptonically $\tau \to \ell\nu_\tau\nu$ and the other decaying hadronically $\tau \to q'\bar{q}\nu_\tau$.

flavor schemes for this process was performed in Ref. [26]. Here, we only note that differences between the two schemes are due to missing higher orders in the truncated perturbative series. Since the perturbative convergence for this process is good, these ambiguities are adequately captured by the scale uncertainty. Interestingly, in contrast to $t\bar{t}H$ and $b\bar{b}H$ production, tqH production includes not only $Hf\bar{f}$ coupling but also HWW coupling [depicted in Figs. 2(b) and 2(d)]. The interference between these diagrams is destructive and leads to a strongly suppressed production rate in the SM [79]. Therefore, any new physics modification of either the $Hf\bar{f}$ or HWW coupling may spoil this suppression and lead to a substantially enhanced production rate and altered kinematics. We therefore include anomalous HWW couplings, following Eq. (4).

The study of spin-zero H boson anomalous couplings to tau leptons relies on the matrix element $H \to \tau^+\tau^-$ with subsequent spin-correlated decays $\tau \to \mu\nu_\tau\nu_\mu$ or $\tau \to q'\bar{q}\nu_\tau$. These decay chains are illustrated in Fig. 3. This decay mode supplements the existing $H \to VV$ decays ($V = W, Z, \gamma, g$) within the JHU generator framework such that any H boson production process can be interfaced with this decay. An option for stable τ leptons allows one to study $H \to \mu^+\mu^-$ or $H \to e^+e^-$ decays as well. Moreover, the tau decay chain encompasses the same structure as the top-quark decay, enabling the future study of fully spin-correlated decay $pp \to X \to t\bar{t} \to b\bar{b}W(\to f'\bar{f})W(\to f'\bar{f})$, where X is any massive spin-zero state. In this work, we will only focus on anomalous coupling studies in $pp \to H \to \tau^+\tau^-$. In the current implementation, the form factors for hadronic tau decay are not implemented in the generator, and instead the inclusive tau decay is simulated. Below, we illustrate the reweighting technique to obtain the $H \to \tau^+\tau^-$ process with anomalous couplings using SM simulation of hadronic τ decays with hadronic form factors by the TAUOLA package [80].

The generation of unweighted events for H boson production in association with heavy-flavor quarks is performed at LO, complemented with parton shower generated by PYTHIA8 [81,82]. The H boson decay is simulated independently from its production. In all cases, the Les Houches Event file format [83] is used to interface the JHU generator program. We also generate weighted events at NLO in QCD for $t\bar{t}H$ production to investigate the impact of radiative corrections, as discussed above. The simulation of the SM processes $t\bar{t}H$ and $b\bar{b}H$ has been checked against the NLO QCD production simulation by POWHEG [84–86], pseudoscalar $t\bar{t}H$ production at NLO QCD has been checked against Ref. [87], and the $H \to \tau^+\tau^-$ decay is validated with TAUOLA. The background $t\bar{t}VV$ samples in this study are generated with MadGraph [88].

TABLE I. Summary of MC processes with anomalous $Hf\bar{f}$ couplings in the production and decay implemented in the JHU generator and the MELA package. The cross sections are listed without systematic uncertainties at the $\sqrt{s} = 13$ TeV LHC for a SM Higgs boson mass of 125 GeV [26,90].

Process	SM cross section or branching	Simulation
$t\bar{t}H$	509 fb	LO + parton shower events NLO QCD weighted events
$b\bar{b}H$	512 fb	LO + parton shower
tqH (t channel)	73 fb	LO + parton shower events
tbH (s channel)	3 fb	LO + parton shower events
$H \to \tau^+\tau^-$	6.3%	LO + parton shower events

In the following, we focus on the LHC energy of $\sqrt{s} = 13$ TeV and use the following input parameters throughout:

$$\begin{aligned} m_H &= 125.0\ \text{GeV}, \qquad m_t = 173.2\ \text{GeV}, \\ m_Z &= 91.19\ \text{GeV}, \qquad m_W = 80.39\ \text{GeV}, \\ m_b &= 4.2\ \text{GeV}, \qquad m_\tau = 1.8\ \text{GeV}, \\ G_\text{F} &= 1.16639 \times 10^{-5}\ \text{GeV}^{-2}, \end{aligned} \tag{5}$$

as well as the NNPDF3.0 parton distribution functions [89]. We summarize the processes relevant to our study of H boson CP properties in heavy-flavor fermion interactions, discussed above, in Table I. We also show their SM production cross sections and the order in perturbative QCD to which they are simulated. For each process shown, we provide the matrix elements through the MELA library. One direct application of MELA is kinematic discriminants for the optimal analysis, as discussed in Sec. IV. This technique also allows one to reweight an existing Monte Carlo sample to any model with anomalous couplings without the need for additional CPU-consuming simulation. This is particularly important for the LHC experiments where modeling ATLAS and CMS detector response sometimes requires months of wall-clock time. A successful application of this procedure has been presented in Ref. [3].

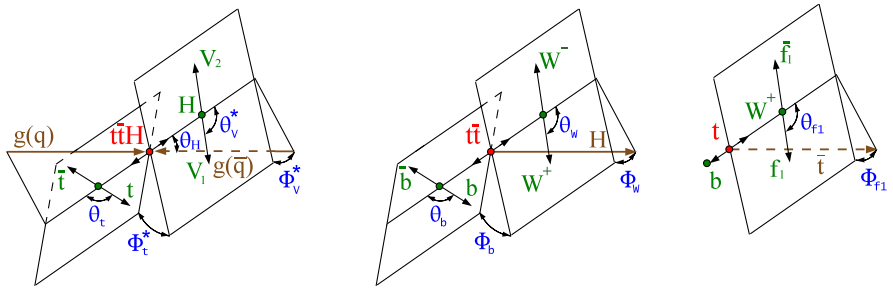

FIG. 4. The definition of observable in the sequential process of production and decay of $t\bar{t}H$; see the text for details. Each angle is defined in the respective reference frame of the decaying system.

IV. MATRIX ELEMENT TECHNIQUE

The matrix elements, or multivariate per-event likelihoods, maximize the amount of information that can be extracted from a given event. These techniques were used for example in top and bottom quarks, as well as electroweak boson measurements, and proved to be powerful tools for the H boson discovery and characterization during Run I of the LHC on both CMS [2,3,41,52,53,55,57,91] and ATLAS [5,59,60] experiments. As part of the latter development, we investigated application of these techniques to the production and decay processes involving H boson coupling to vector bosons in Refs. [61–63]. Here, we extend the MELA technique to the processes involving H boson coupling to heavy-flavor fermions.

We take the $gg(q\bar{q}) \to t\bar{t}H$ processes as an example to define a complete set of kinematic observables following the full sequence of the process, similar to the HVV production and decay kinematics discussed in Refs. [61,63]. These observables are equivalent to the more familiar observables defined in the laboratory frame, as shown in Appendix, but provide a more intuitive insight into the production and decay dynamics. We then define the complete set of matrix element discriminants, following Refs. [62,63], in application to the processes involving heavy fermion couplings to the H boson.

A. Kinematics in the H boson production and decay

The processes $gg(q\bar{q}) \to t\bar{t}H$, tqH, or $b\bar{b}H$ with subsequent decay of the top quarks and the H boson can be characterized by the 4-momenta of the decay products, such as leptons and quark jets. In the case of one final-state neutrino, its momentum can be deduced from a kinematic fit using mass constraints and utilizing the missing transverse energy information. In the following description, we consider the $t\bar{t}H$ production in its center-of-mass frame. Both longitudinal and transverse momenta of the $t\bar{t}H$ system can be parametrized separately. They are driven by QCD effects, either parton distribution functions of the proton for rapidity or additional jet radiation for transverse momentum.

Similar to the description of the H boson production and decay with couplings to vector bosons [61–63], it is convenient to describe the complete kinematics of the process by a set of angles and invariant masses, which we generically denote as $\vec{\Omega}$, following the sequential processes. The definition of observables in the process $gg(q\bar{q}) \to t\bar{t}H \to (W^+b)(W^-\bar{b})H \to (f'_1\bar{f}_1b)(\bar{f}_2f'_2\bar{b})(VV)$ is shown in Fig. 4. The following set of angles and invariant masses is defined as:

(i) $m_{t\bar{t}H}$: invariant mass of the $t\bar{t}H$ system;
(ii) θ_H: angle between the H boson direction and the incoming partons in the $t\bar{t}H$ frame;
(iii) θ^*_V: angle of the $H \to VV(f\bar{f})$ decay with respect to the opposite $t\bar{t}$ direction in the H frame;
(iv) Φ^*_V: angle between the production plane, defined by incoming partons and H, and $H \to VV(f\bar{f})$ decay plane;
(v) θ_t: angle between the top-quark direction and the opposite Higgs direction in the $t\bar{t}$ frame;
(vi) Φ^*_t: angle between the decay planes of the $t\bar{t}$ system and $H \to VV(f\bar{f})$ in the $t\bar{t}H$ frame;
(vii) m_{tt}: invariant mass of the $t\bar{t}$ system;
(viii) θ_W: angle between W^+ and opposite of the $b\bar{b}$ system in the W^+W^- frame;
(ix) Φ_W: angle between the production $(b\bar{b})(W^+W^-)H$ plane and the plane of the W^+W^- system in the $t\bar{t}$ frame;
(x) θ_b: angle between the b quark and opposite of the W^+W^- system in the $b\bar{b}$ frame;
(xi) Φ_b: angle between the planes of the $b\bar{b}$ and W^+W^- systems in the $t\bar{t}$ frame;
(xii) m_{Wb1} or m_{Wb2}: invariant mass of the W^+b or $W^-\bar{b}$ system;
(xiii) θ_{f1} or θ_{f2}: angles between fermion direction and opposite of the b or $\bar{b}$ quark in the W^+ or W^- frame;
(xiv) Φ_{f1} or Φ_{f2}: angle between the W^+ or W^- decay plane and the $\bar{t}W^+b$ or $tW^-\bar{b}$ plane in the t or $\bar{t}$-quark frame;
(xv) $m_{f1\bar{f}1}$ or $m_{f2\bar{f}2}$: invariant mass of the $f_1\bar{f}_1$ or $f_2\bar{f}_2$ system.

The decay of the H boson with angles θ^*_V and Φ^*_V is shown only for illustration; their distribution is flat for a spin-zero H boson production due to the lack of spin correlations between the production and decay processes. Their complete description is discussed in Ref. [61] in terms of the

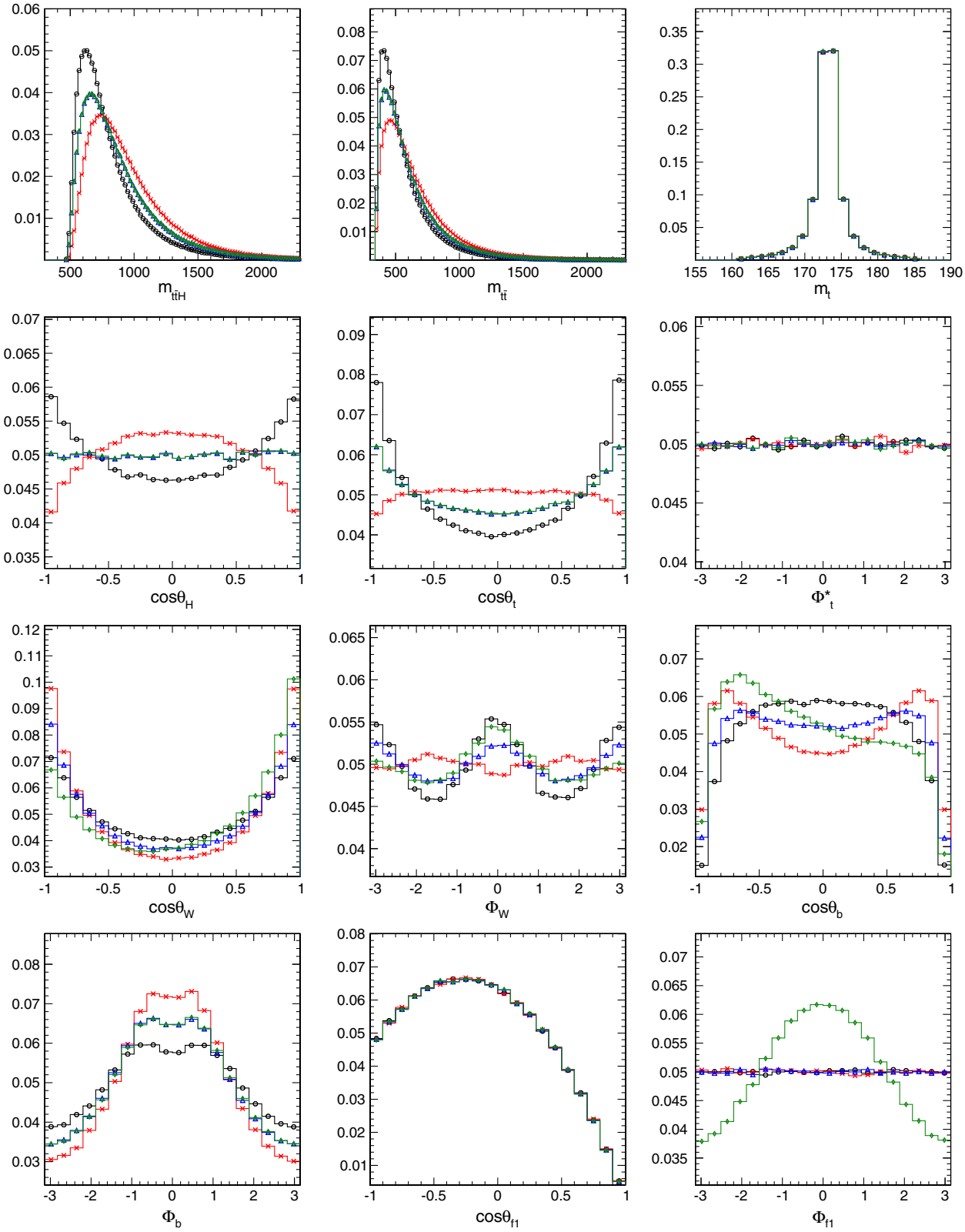

FIG. 5. The normalized angular and mass distributions in the process $pp \to t\bar{t}H$ corresponding to four scenarios of anomalous $t\bar{t}H$ couplings: $f_{CP} = 0$ (SM 0^+, red crosses), $f_{CP} = 1$ (pseudoscalar 0^-, black circles), $f_{CP} = 0.28$ with $\phi_{CP} = 0$ (blue triangles), and $\phi_{CP} = \pi/2$ (green diamonds). The LHC pp energy of 13 TeV and H boson mass of 125 GeV are used in simulation. See the text for the definition of all observables.

two equivalent angles θ^* and Φ_1. The grouping of the W^+W^- and $b\bar{b}$ systems, as opposed to W^+b and $W^-\bar{b}$, is motivated by enhanced spin-correlation effects visible with the corresponding observables. The complete multidimensional distribution retains full information with either approach.

Figure 5 shows the nontrivial angular distributions in the process $pp \to t\bar{t}H$ corresponding to four scenarios of anomalous $t\bar{t}H$ couplings: pure scalar, pseudoscalar, and two mixed scenarios with $f_{CP} = 0.28$ (corresponding to the equal cross section of scalar and pseudoscalar processes) and different phases. Most angular observables exhibit a clear difference between the scalar and pseudoscalar processes. Only observables appearing in sequential decay of the top quarks are sensitive to ϕ_{CP}. As noted earlier, these observables together with the boost of the $t\bar{t}H$ system are equivalent to other observables defined in the laboratory frame, as shown in Appendix, but provide complete kinematics required as input to the matrix element tools and emphasize particular features in the process.

The description of observables $\vec{\Omega}$ in the other processes $pp \to tqH$ and $b\bar{b}H$ follows by analogy, with only a subset of observables available due to lack of sequential decay of at least one associated quark.

B. Matrix element likelihood approach

With the kinematics of a process reflected in the complete set of observables $\vec{\Omega}$, one could in principle analyze the data in this multidimensional space. However, this often becomes impractical with a large number of observables, as illustrated in Sec. IV A, when parametrization of probabilities and detector effects in such a multidimensional space becomes difficult. Reducing the number of observables is a possible approach, but essential information may be lost. Machine learning techniques can approximate optimal functions that can depend on a large number of inputs, but those also require training and therefore perform only as well as training goes. These techniques are typically targeted to discriminate between certain categories of events and are not optimal for dealing with quantum mechanical interference effects which become essential in physics processes; though for possible solutions, see Ref. [92].

The matrix element techniques are the methods based on multivariate per-event likelihoods prepared using a phenomenological calculation for the process of interest. They may employ the same calculation as used in the Monte Carlo event generators or may be reformulated to represent analytical distributions of observables of interest, such as $\vec{\Omega}$. Such matrix elements, if used properly, are guaranteed to retain full information about the event. The difficulty in using matrix element methods often comes from nontrivial detector effects which alter multivariate likelihoods. This difficulty is greatly reduced by utilizing ratios of the matrix elements. In the ratios, certain detector effects cancel, such as variation of reconstruction efficiency. Resolution effects may be introduced with transfer functions or neglected when their effect on performance is small. Missing degrees of freedom, such as neutrinos, may be either constrained from the global event information, as we illustrate below, or integrated out in the matrix element calculation. In the end, either machine learning or matrix element techniques could be used in the analysis of the data, but in either approach, it is ultimately the matrix elements which guide us in maximizing the amount of information, as they are also used in machine training through Monte Carlo.

The basic idea of the MELA technique is to project kinematics on the minimal set of discriminants calculated as ratios of the matrix elements. It has already proven to be a powerful tool for the H boson discovery and characterization during Run I of the LHC as applied primarily to the H boson coupling to the vector bosons. For a simple discrimination of two hypotheses, the Neyman-Pearson lemma [93] guarantees that the ratio of probabilities $\mathcal{P}$ for the two hypotheses provides an optimal discrimination power. However, for a continuous set of hypotheses with an arbitrary quantum-mechanical mixture, several discriminants are required for an optimal measurement of their relative contributions. For example, probability for interference of two contributions could be presented as

$$\begin{aligned}\mathcal{P}_{\rm sig}(\vec{x}_i; f_{CP}, \phi_{CP}) = {} & (1-f_{CP})\mathcal{P}_{0^+}(\vec{x}_i) + f_{CP}\mathcal{P}_{0^-}(\vec{x}_i) \\ & + \sqrt{f_{CP}(1-f_{CP})}(\mathcal{P}_{\rm int}(\vec{x}_i)\cos\phi_{CP} \\ & + \mathcal{P}^{\perp}_{\rm int}(\vec{x}_i)\sin\phi_{CP}),\end{aligned} \tag{6}$$

where $\mathcal{P}_{\rm int}$ and $\mathcal{P}^{\perp}_{\rm int}$ describe quantum mechanical interference of $J^P = 0^+$ and 0^- terms. One could apply the Neyman-Pearson lemma to each pair of points in the parameter space of (f_{CP}, ϕ_{CP}), but this would require a continuous, and therefore infinite, set of probability ratios. However, equivalent information is contained in a linear combination of only three probability ratios, which can be treated as three independent observables. For H boson physics at proton or lepton colliders, such discriminants are introduced in Ref. [63] as

$$\mathcal{D}_{0-} = \frac{\mathcal{P}_{0^+}(\vec{\Omega})}{\mathcal{P}_{0^+}(\vec{\Omega}) + \mathcal{P}_{0^-}(\vec{\Omega})}, \tag{7}$$

$$\mathcal{D}_{CP} = \frac{\mathcal{P}_{\rm int}(\vec{\Omega})}{\mathcal{P}_{0^+}(\vec{\Omega}) + \mathcal{P}_{0^-}(\vec{\Omega})}, \tag{8}$$

$$\mathcal{D}^{\perp}_{CP} = \frac{\mathcal{P}^{\perp}_{\rm int}(\vec{\Omega})}{\mathcal{P}_{0^+}(\vec{\Omega}) + \mathcal{P}_{0^-}(\vec{\Omega})}, \tag{9}$$

which become the optimal discriminants for the process with four contributions in Eq. (6).

In Eq. (6), $\vec{x}_i$ is a set of observables describing the process, which may be $\vec{\Omega}$ when calculating the discriminants, or may be discriminants themselves when performing the analysis later. The number of discriminants can also be reduced by dropping $\mathcal{D}_{CP}^{\perp}$ assuming $\sin\phi_{CP} = 0$, which is the case for real κ_f and $\tilde{\kappa}_f$ in Eq. (2). On the other hand, with additional contributing amplitudes, the number of observables grows. For example, in the presence of background, the $\mathcal{D}_{\rm bkg}$ discriminant is introduced which can also be supplemented by the interference discriminant if there is quantum mechanical interference between the signal and background processes. The corresponding two discriminants are defined as

$$\mathcal{D}_{\rm bkg} = \frac{\mathcal{P}_{0^+}(\vec{\Omega})}{\mathcal{P}_{0^+}(\vec{\Omega}) + \mathcal{P}_{\rm bkg}(\vec{\Omega})}, \tag{10}$$

$$\mathcal{D}_{\rm bkg}^{\rm int} = \frac{\mathcal{P}_{\rm int}^{\rm bkg}(\vec{\Omega})}{\mathcal{P}_{0^+}(\vec{\Omega}) + \mathcal{P}_{\rm bkg}(\vec{\Omega})}. \tag{11}$$

Calculating a discriminant analogous to $\mathcal{D}_{\rm bkg}$ for the pseudoscalar signal hypothesis is not necessary as a combination of Eqs. (7) and (10) carries the needed information. The number of discriminants grows with the number of free components in the model; for example, the background may interfere with different signal components, and those may require different observables. However, typically there is a limited set of interference discriminants which become of practical interest, as we illustrate below.

The probabilities $\mathcal{P}$ in Eqs. (7)–(11) are the physical cross sections given by the product of parton distribution functions convoluted with the partonic cross sections that are proportional to the squared matrix elements. The latter depend on the full event kinematics as measured in the experiment or simulated by a Monte Carlo generator. They are computed at LO and do not include detector effects. However, as we illustrate in the following studies, they remain nearly optimal even after higher-order or detector effects are introduced. The probabilities $\mathcal{P}$ in Eq. (6) may be treated as templates of the limited number of optimal discriminants when the analysis is performed. These templates are obtained from numerical simulation of the processes accounting for parton showering and detector effects. In the following analysis, we limit the maximum number of discriminants to three, which we find to be both practical and close to optimal.

The complete set of optimal discriminants in Eqs. (7)–(11) was introduced earlier in experimental analysis of HVV processes with LHC data by the CMS [2,3,52,53,55,57,91] and ATLAS [5,59,60] experiments and phenomenological studies supporting this development [61–63]. For example, it was shown that the complete set $x_i = \{\mathcal{D}_{0-}, \mathcal{D}_{CP}, \mathcal{D}_{\rm bkg}\}$ was optimal for the measurement of f_{a3}, a parameter equivalent to f_{CP}, for the real HVV couplings. A subset of equivalent observables was also introduced independently in earlier work on different topics [94–96]. Here, we apply this formalism to the measurement of the H boson anomalous couplings to the heavy-flavor fermions for the first time.

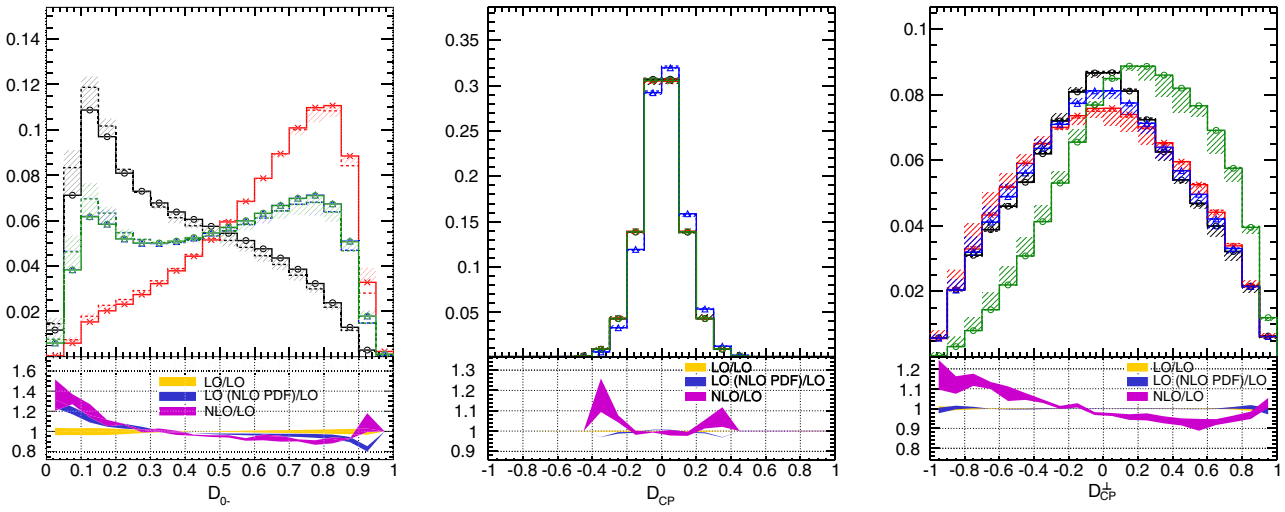

FIG. 6. Top: the D_{0-} (left), $\mathcal{D}_{CP}$ (middle), and $\mathcal{D}_{CP}^{\perp}$ (right) discriminant distributions for the $t\bar{t}H$ process for the H boson models $J^P = 0^+$ (red crosses), 0^- (black circles), $f_{CP} = 0.28$ with $\phi_{CP} = 0$ (blue triangles), and $\phi_{CP} = \pi/2$ (green diamonds). The solid histogram shows distributions generated at LO in QCD. The hatched region covers the range between LO and NLO distributions. The dashed histograms shows distributions generated with the LO matrix element and NLO PDFs. Bottom: ratios of distributions for $f_{CP}\cos(\phi_{CP}) = 0.28$ with the ranges corresponding to the QCD scale variations, where the denominator is the distribution generated at LO without considering scale variations. The LO/LO ratio is centered around 1, and its width is the effect of scale variation. The LO (NLO PDF)/LO ratio includes distribution generated with LO matrix element and NLO PDFs. The NLO/LO ratio includes distribution generated at NLO.

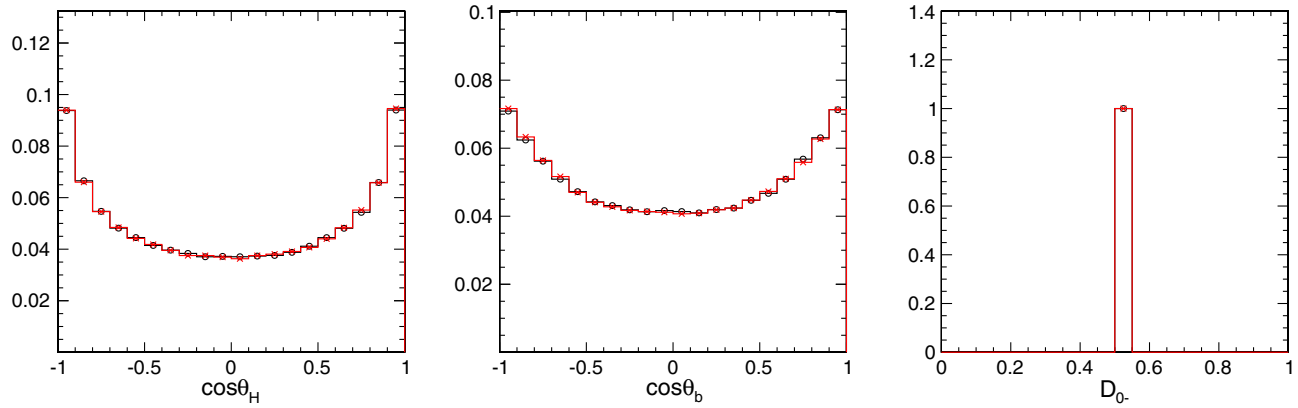

FIG. 7. Distributions for the $b\bar{b}H$ process: $\cos\theta_H$ (left), $\cos\theta_b$ (middle), and D_{0-} discriminant (right) for $J^P = 0^+$ (black circles) and 0^- (red crosses).

C. Application to the $t\bar{t}H$ process

The large number of observables $\vec{\Omega}$ defined in Sec. IV A for the $t\bar{t}H$ process can be compressed in a compact form with only three discriminants $x_i = \{\mathcal{D}_{0-}, \mathcal{D}_{CP}, \mathcal{D}_{CP}^{\perp}\}$ as defined in Eqs. (7)–(9), which is sensitive to the measurement of anomalous $t\bar{t}H$ couplings. The distributions for the discriminants are shown in Fig. 6 for $J^P = 0^+$, 0^-, and mixed states. The nominal studies presented here are based on LO in QCD calculations. Variations due to NLO matrix elements, parton distribution functions (PDFs), and QCD scale uncertainties are also shown in Fig. 6 and are discussed in more detail in Sec. V.

As one can see from both the discriminant definitions and distributions in Fig. 6, the $\mathcal{D}_{0-}$ is sensitive to the relative size of CP contributions, while $\mathcal{D}_{CP}$ and $\mathcal{D}_{CP}^{\perp}$ are sensitive to CP mixture leading to forward-backward asymmetry in the presence of both CP amplitudes for the real and complex ratio of couplings $\kappa_f/\tilde{\kappa}_f$, respectively. It is interesting to observe that the asymmetry is not strongly pronounced in the case of real couplings even when using the full top decay chain information. The asymmetry is more pronounced in the case of complex couplings, as seen in the $\mathcal{D}_{CP}^{\perp}$ distribution, which can be traced to the Φ_{f1} distribution in Fig. 5. The asymmetry in both $\mathcal{D}_{CP}$ and $\mathcal{D}_{CP}^{\perp}$ disappears when top decay information is not used in the matrix element, which reflects the fact that spin correlations in the $t\bar{t}$ system decay are essential for observing effects sensitive to CP mixture.

At the moment of discovery of the $t\bar{t}H$ process, precision will be limited by statistics, and the $\mathcal{D}_{0-}$ discriminant will provide the most information about the CP components in the process. As smaller anomalous contributions get tested, the importance of the interference discriminant will grow, but ultimately the full information is contained in the complete set of discriminants.

D. Application to the $b\bar{b}H$ process

The $b\bar{b}H$ and $t\bar{t}H$ processes are very similar with the main difference being the heavy-quark mass which, in fact, has a significant impact on the sensitivity of kinematic shapes to the $Hf\bar{f}$ couplings. This is because shape sensitivity arises from the mixing of left- and right-handed helicities at the matrix element level. Therefore, this effect becomes proportional to the mass of the associated quark and becomes essentially invisible in the $b\bar{b}H$ process. In Fig. 7, we plot the angular distributions as well as the matrix element discriminant for the $b\bar{b}H$ process, analogous to $t\bar{t}H$ process distributions shown in Figs. 5 and 6. The different CP states have almost identical distributions, as follows from the helicity flip suppression discussed above. Therefore, we conclude that it will be very challenging to probe the CP nature of $Hb\bar{b}$ coupling through shape analyses in the $b\bar{b}H$ production mode.

E. Application to the tqH process

The tqH production process features both fermion and vector boson couplings of the H boson, as shown in Fig. 2. Interference between the $Hf\bar{f}$- and HVV-induced diagrams in Fig. 2 is destructive in the SM, but any deviation in either size or sign of either contribution could lead to a significant change in observations. Therefore, in this paper, we illustrate the approach where two parameters of interest are determined: relative size of the $Hf\bar{f}$ and HVV contributions, including their relative phase, and the relative size of the anomalous $Hf\bar{f}$ coupling. In this context, contributions from the HVV process could be considered as background, and we consider only SM-like HVV coupling with $a_1 \neq 0$ in Eq. (4), while the signal process with the $Hf\bar{f}$ coupling is allowed to have an arbitrary anomalous contribution. Therefore, the three discriminants $\mathcal{D}_{0-}$, $\mathcal{D}_{\rm bkg}$, and $\mathcal{D}_{\rm bkg}^{\rm int}$ as defined in Eqs. (7), (10), (11) provide the most relevant information for this analysis. Their distributions are shown in Fig. 8.

There is a clear difference between distributions for the alternative hypotheses, such as between $J^P = 0^+$ and the $0 - Hf\bar{f}$-induced signal in $\mathcal{D}_{0-}$ or between $J^P = 0^+$ signal and the HVV-induced process in $\mathcal{D}_{\rm bkg}$. It is important to

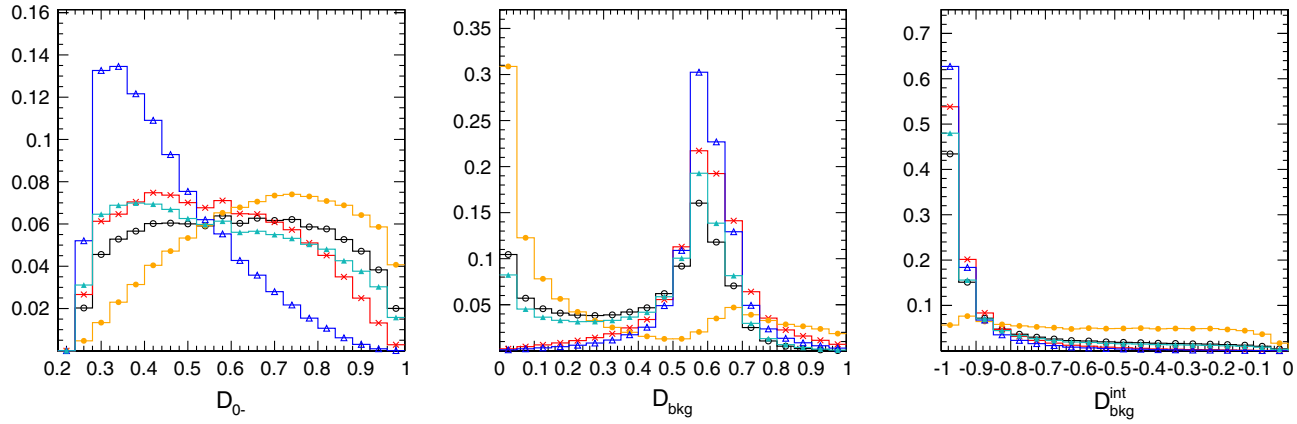

FIG. 8. Distributions of $\mathcal{D}_{0-}$ (left), $\mathcal{D}_{\rm bkg}$ (middle), and $\mathcal{D}^{\rm int}_{\rm bkg}$ (right) discriminants for the tqH production process, where five contributions are considered: $Hf\bar{f}$ coupling as $J^P = 0^+$ signal (red crosses) or as 0^- signal (blue triangles); HVV-induced process as background (black circles); the sum of $Hf\bar{f}$ and HVV processes, including interference, with 0^+ $Hf\bar{f}$-induced signal (orange closed circles); or 0^- $Hf\bar{f}$-induced signal (cyan triangles).

stress that destructive interference between the $J^P = 0^+$ signal and HVV-induced processes with SM couplings leads to distributions which are very different from the direct sum of the two distributions, as shown in Fig. 8. In particular, the $\mathcal{D}^{\rm int}_{\rm bkg}$ discriminant shape is significantly distorted due to the effect of interference, while the other two discriminants also exhibit sizable differences as well. This feature leads to strong separation power between different hypotheses even with a small number of events in analysis, as we show below.

F. Application to the $H \to \tau^+\tau^-$ process

In the $H \to \tau^+\tau^-$ process, it is possible to define the full sequential decay kinematics and construct the matrix elements using information about all final-state particles. This is illustrated for the process $H \to \tau^+\tau^- \to (\ell\nu\nu)(\ell\nu\nu)$ with the D_{0-} discriminant in Fig. 9. Even though there is a strong separation power between the $J^P = 0^+$ and 0^- models in this case, there is little practical application because reconstruction of the four neutrinos is not possible. Therefore, only limited information can be retained in reconstructed observables, and we use the matrix elements for the purpose of MC reweighting techniques below.

In the case of hadronic τ decay, we provide the matrix element for the $H \to \tau^+\tau^- \to (X\nu)(X'\nu)$ process, where X could be any hadronic particle decayed from τ, e.g., π, ρ, a_1. Figure 10 shows the D_{0-} discriminant constructed using this matrix element, in a hadronic final state. The events are decayed through TAUOLA, including hadronic form factors for particle hadronization, for the $J^P = 0^+$ and 0^- models. In addition, the $J^P = 0^+$ events are reweighted to the 0^- model using the MELA weights, which allow us to create any model with arbitrary anomalous couplings. The D_{0-} discriminant can be compared to other observables proposed for analysis of the $H \to \tau^+\tau^-$ decay, for example, Φ_{CP} [36], defined as

$$\Phi_{CP} = \text{acos}(\vec{n}_X \cdot \vec{n}_{X'}); \quad \text{where } \vec{n}_X = \frac{\vec{q}_X \times \vec{q}_{\tau-}}{|\vec{q}_X \times \vec{q}_{\tau-}|}, \tag{12}$$

and $\vec{q}_{\tau^-}$ and $\vec{q}_{X,X'}$ are the 3-momentum of τ^- and X or X' in the H boson rest frame. The two observables, D_{0-} and Φ_{CP}, carry similar information for analysis of anomalous couplings, but the D_{0-} discriminant is somewhat more powerful.

V. NLO QCD STUDY OF KINEMATIC DISCRIMINANTS

Let us now discuss the effects of higher-order QCD corrections on the modeling and performance of anomalous coupling discrimination. As described in Sec. III, we compute the NLO QCD predictions for $pp \to t\bar{t}H$ production followed by the spin-correlated top-quark decays at NLO QCD in the narrow-width approximation.

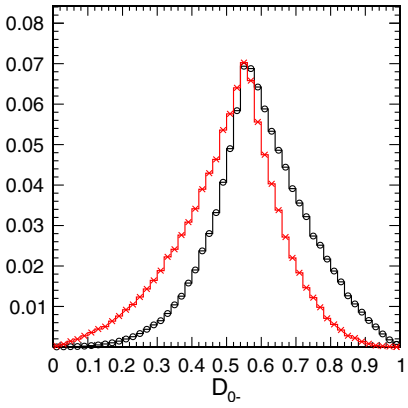

FIG. 9. Distributions of the D_{0-} discriminant for $J^P = 0^+$ (black circles) and 0^- (red crosses) models in the ideal process $H \to \tau^+\tau^- \to (\ell\nu\nu)(\ell\nu\nu)$ simulated by JHUGen and assuming all final-state particles are reconstructed.

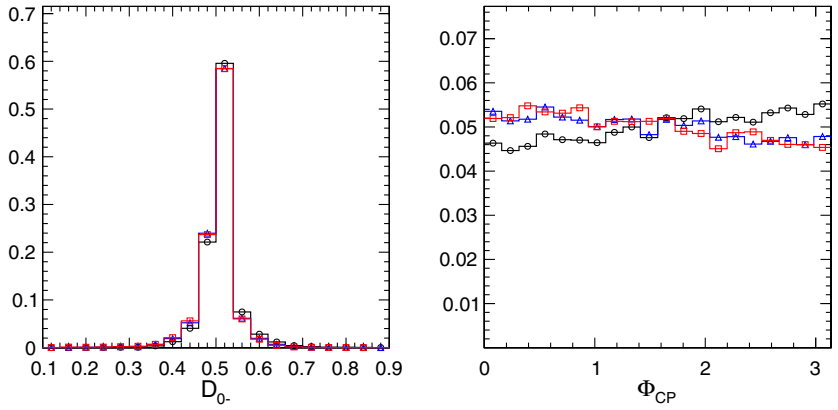

FIG. 10. The distributions of D_{0-} (left) and Φ_{CP} (right) for $H \to \tau\tau \to (X\nu)(X'\nu)$ simulation, where X is a hadronic state. The $J^P = 0^+$ (black circles) and 0^- (red squares) distributions are generated with TAUOLA, including hadronic form factors, and the 0^- (blue triangles) distributions are obtained from the 0^+ simulation using MELA reweighting.

Neglecting QCD corrections in the description of the $pp \to t\bar{t} + H$ process constitutes the dominant theoretical uncertainty on its cross section. We find that residual scale uncertainty on the total cross section is reduced from 21% to 9% when going from LO to NLO in QCD. The corrections on shapes of basic kinematic distributions are up to $\pm 10\%$.

In the earlier work [63], we studied the impact of NLO in QCD effects in production on the anomalous coupling discrimination in decay $H \to VV$. However, the production and decay processes carry no spin correlation, and additional radiation from the production stage is largely decoupled from the color-neutral $H \to VV$ decay dynamics. Hence, it is straightforward to use LO matrix elements to characterize HVV couplings, even in the presence of initial-state radiation. This is in contrast to the $pp \to t\bar{t}(\to b\bar{b}WW) + H(\to VV/f\bar{f})$ process where initial- and final-state particles radiate color charges and the top quarks exhibit spin correlations, all of which affect the studied dynamics.

A fully consistent extension of the matrix element method beyond the LO requires both event generation and matrix element discriminants at higher orders. The main complication stems from kinematic configurations where hadronic activity is clustered by a jet algorithm. Commonly used jet algorithms combine soft and collinear radiation in subsequent $2 \to 1$ recombination steps. Hence, the resulting jet either acquires some invariant mass which does not correspond to the fundamental parton mass or the jet violates global momentum conservation. This feature prohibits the use of jet momenta in a LO matrix element, which has on-shell-ness (of quarks and gluons) and momentum conservation built in from first principles. A systematic solution to this issue at NLO QCD is part of active research, and first elegant solutions have been presented in Refs. [97–100], where modified jet algorithms are proposed to map resolved and unresolved parton configurations onto their proper matrix elements. These approaches have promising prospects for future measurements, but they require the use of new jet algorithms that are currently not used in experimental analyses. Moreover, only solutions for either colorless final states or colorless initial states have been presented in the literature. A fully developed application to, e.g., top-quark pair production at NLO QCD is not yet available. A variation away from the exact NLO treatment has also been presented in Ref. [101], where additional radiation is included through a parton shower approximation. This approach allows one to include multiple emissions and has been applied to Higgs boson physics in Refs. [102,103].

In this paper, we take a pragmatic and more simplistic approach. We retain leading-order matrix elements in the discriminants of Eqs. (7)–(11) and probe them with events from leading- *and* next-to-leading-order simulation and also compare those to variations due to PDFs, QCD scales, and parton showering. The mismatch between the LO discriminants and NLO simulation does not formally allow us to claim optimal discrimination power by virtue of the Neyman-Pearson lemma, where constructed likelihoods should be interpreted as fundamental probabilities. However, we demonstrate that NLO corrections to the shapes of kinematic distributions in the $pp \to t\bar{t}H$ process are small and sometimes indistinguishable when compared to other associated uncertainties. Therefore, the LO discriminants $\mathcal{D}$ maintain their discriminating power beyond the well-defined leading order, and we can continue to use them as robust and powerful tools for anomalous coupling studies.

In Fig. 6, we compare the impact of LO vs NLO events probing the LO discriminants $\mathcal{D}$. The solid histograms show the distribution for LO events, whereas the hashed bands indicate the shift due to NLO corrections. We note that the general shapes of the various distributions are maintained and only minimally distorted. The separation power between the extreme $J^P = 0^+$ and 0^- hypotheses is largely unaffected by the presence of higher-order corrections. The most powerful discriminating observable

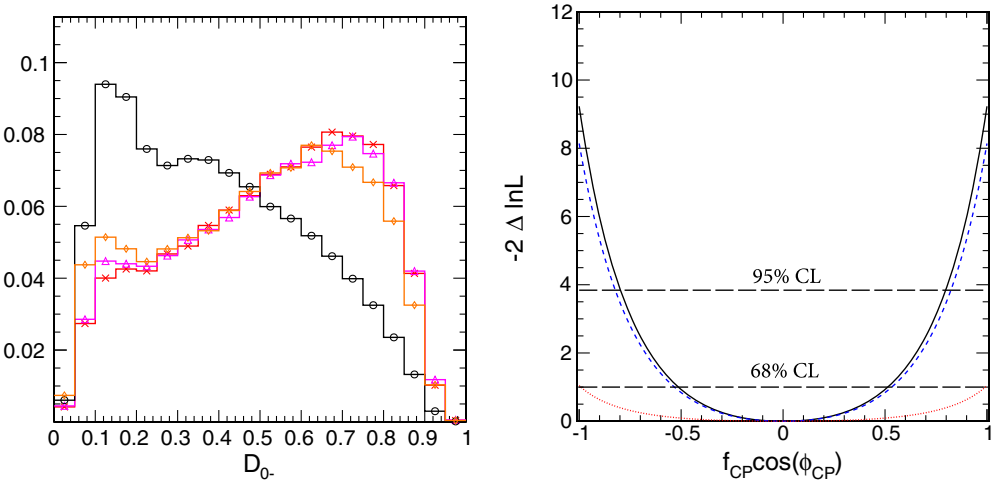

FIG. 11. Left: the $\mathcal{D}_{0-}$ discriminant distribution for $t\bar{t}H$, $H \to \gamma\gamma$ process after reconstruction discussed in the text. The following distributions are shown: $Hf\bar{f}$ coupling as $J^P = 0^+$ signal (red crosses) and as 0^- signal (black circles) and $tt\gamma\gamma$ background (orange diamonds). Also shown is the SM $J^P = 0^+$ signal generated at NLO in QCD with POWHEG (magenta triangles). Right: the likelihood scan of $f_{CP}\cos(\phi_{CP})$, where $\phi_{CP} = 0$ or π, in the $t\bar{t}H$ process with both $H \to \gamma\gamma$ (blue dashed) and $H \to 4\ell$ (red dotted) decays, and the combined result (solid black) expected with 300 fb^{-1} at LHC.

$\mathcal{D}_{0-}$ receives very small corrections in range within the bulk of the distributions, as shown in the lower pane of Fig. 6. Moreover, most of this correction appears already with the PDF variations before NLO corrections at the matrix element level. Hence, the bulk of corrections that we observe stems only from different input parameters and PDFs. The width of the bands in all lower panes of Fig. 6 corresponds to scale variations by a factor of 2 around the central scale $\mu = m_t + m_H/2$. Studies presented in Fig. 6 do not include parton showering. However, as we show in Sec. VI A and Fig. 11, inclusion of parton showering in LO simulation brings this simulation even closer to NLO modeling with parton showering.

We therefore conclude that discrimination power of the MELA approach is guaranteed even when higher-order corrections are considered in the $pp \to t\bar{t}H$ process and additional jets are present in the event sample. Soft and collinear radiation, which generates massive jet momenta, can be handled in the matrix element approach and does not spoil the discrimination power. These higher-order effects are within the uncertainties of the PDF, scale choice, and parton showering.

VI. APPLICATION TO *CP* PARITY MEASUREMENTS IN $t\bar{t}H$, tqH, AND $b\bar{b}H$

In this section, we estimate the potential for CP measurements in the $t\bar{t}H$, tqH, and $b\bar{b}H$ processes on the LHC with 300 fb^{-1} of proton-proton collision data collected at 13 TeV center-of-mass energy. This is the integrated luminosity expected by the end of Run III of the LHC in about 7 years. Projections to other luminosity scenarios are usually trivial extensions as long as uncertainties remain limited by statistics. While there is a strong evidence for the $t\bar{t}H$ production in Run I of LHC, none of these processes has been firmly established yet. However, we rely on experimental studies of these processes in Refs. [39–43] for realistic event reconstruction projections.

As the first observation, following Sec. IV D, we conclude that it will not be possible to measure CP in the $b\bar{b}H$ production process in the LHC program. For the $t\bar{t}H$ and tqH processes, we consider the $H \to \gamma\gamma$ decay mode to tag the H boson, as a clean signature with sizable branching fraction. We also consider the $H \to ZZ \to 4\ell$ final state in the $t\bar{t}H$ process for comparison, but its contribution is small due to the small branching fraction. We use the hadronic decay of one top-quark final state so that the full kinematics can be reconstructed. In the $t\bar{t}H$ case, the other top quark is reconstructed in the leptonic channel. Inclusion of other final states of either the H boson or top would only enhance expected precision, but the decays we consider are representative of the typical analyses of these processes.

In this study, the $t\bar{t}H$, $b\bar{b}H$, and tqH processes with SM or anomalous couplings are generated with the JHU generator. The only non-negligible background that we need to consider is SM $t\bar{t}\gamma\gamma$ production as a background to the $t\bar{t}H$ study with the photon decay of the H boson, which is simulated with MadGraph. The MC samples are interfaced to PYTHIA8 for parton shower and hadronization. In order to model detector effects, the lepton and photon p_T are smeared with 1% and 4% resolution. The jets are reconstructed in a cone of $R = 0.5$ using an anti-k_T algorithm, and their energy is smeared by 20%.

The event selection criteria follow those of the LHC analyses [40]. We require the leptons, photons, and jets to have $p_T > 5$, 10, and 30 GeV and $|\eta| < 2.4$, 2.4, and 4.7,

TABLE II. Number of events expected in the SM for signal and other contributions in the study of $Hf\bar{f}$ couplings discussed in text with 300 fb^{-1} at 13 TeV.

Signal process	Signal yield	Other process	Other yield
$t\bar{t}H$, $H \to \gamma\gamma$	50.3	$t\bar{t}\gamma\gamma$	100.6
$t\bar{t}H$, $H \to 4\ell$	4.3	Negligible	0
tqH, $H \to \gamma\gamma$	3.2	$t\bar{t}H$, $H \to \gamma\gamma$	10.2

respectively. Jets within $\Delta R < 0.2$ of the leptons or photons are removed. In the $t\bar{t}H$ analysis, an event should have at least four jets and a b-tagged jet. The b-tagging efficiency (62%) and fake rate for the light-quark jets (6%) follow experimental study [40]. To fully reconstruct the semileptonic decay of the $t\bar{t}$ system, we use the constraint fit from Ref. [104]. The 4-momenta of four jets, missing transverse energy, and one lepton are used in the kinematic fit with the masses of the top quarks and the W bosons as constraints. If more than four jets are reconstructed, the combination that gives the best χ^2 is selected. The 4-momenta of all decay products of the $t\bar{t}$ system are obtained from this fit and are used in the further analysis. In the tqH analysis, exactly four jets and a b-tagged jet are required in order to remove hadronic $t\bar{t}H$ events. The combination of three jets with the mass closest to the top is treated as the top decay product in this process. The required number of reconstructed leptons and photons depends on the studied final state. If required, the leading photon should have $p_T > 33$ GeV and $p_T/m_{\gamma\gamma} > 0.5$. In the $H \to 4\ell$ channel, two pairs of opposite sign and same flavor leptons should have invariant mass greater than 40 and 12 GeV. The invariant mass of the H boson candidate is required to be between 100 and 140 GeV.

In the case of the tqH process with $H \to \gamma\gamma$, the main other contribution is cross-feed from the $t\bar{t}H$ process with the same H boson decay. The $t\bar{t}H$ process with the 4ℓ decay of the H boson has negligible background, while with the $\gamma\gamma$ decay, the dominant background is the SM $t\bar{t}\gamma\gamma$ production. The expected number of events of signal and background events at 300 fb^{-1} is shown in Table II. We would like to note that these expected yields are quoted for the SM scenario where destructive interference between the $Hf\bar{f}$- and HVV-induced tqH processes leads to a small number of expected events. However, this interference may become constructive with the non-SM couplings. The cross section for $t\bar{t}\gamma\gamma$ processes suggests background yield to be smaller than the signal. However, the LHC studies with data-driven methods suggest larger background [40]. Therefore, we conservatively set the $t\bar{t}\gamma\gamma$ background yield to be twice the signal in the invariant mass window specified above.

A. Study of the $t\bar{t}H$ process

The analysis of the $t\bar{t}H$ process uses the $\mathcal{D}_{0-}$ discriminant, where decay of the top quarks is not considered in the matrix element. Consideration of the top-quark decays is important in the calculation of the $\mathcal{D}_{CP}$ or $\mathcal{D}_{CP}^{\perp}$ discriminants, but only when the up and down flavors of the quarks in the decay chain are known. The latter is difficult to determine with the jet reconstruction techniques, and therefore the CP discriminants are not used in this analysis. In the $H \to \gamma\gamma$ channel, we use the invariant mass $m_{\gamma\gamma}$ to separate the signal and background. Figure 11 shows the $\mathcal{D}_{0-}$ distribution in the $H \to \gamma\gamma$ channel, where the $J^P = 0^+$, 0^- and background distributions are shown.

In Fig. 11, simulation of the 0^+ process is also shown with the POWHEG generator at NLO in QCD. In all cases, parton showering is performed with PYTHIA8. Similar to the study presented in Sec. V, the NLO QCD effects are found to have a small effect on the accuracy of $\mathcal{D}_{0-}$ simulation, especially after parton showering is included in simulation. Any residual effects are consistent with systematics also arising from PDF and QCD scale variations.

The expected precision of the f_{CP} measurement in the $t\bar{t}H$ process with both $H \to \gamma\gamma$ and $H \to 4\ell$ decays, and their combination, is shown in Fig. 11 for an integrated luminosity of 300 fb^{-1}. The maximum likelihood fit is based on the probability density functions following Eq. (6) parametrized with template distributions filled with generated events as discussed above. About 3σ exclusion of the pure pseudoscalar state is expected in such a scenario, which is comparable to the current precision with the HVV measurements, but provides a fundamentally different approach through fermion couplings. Scenarios with a sizable CP mixture, $|f_{CP}\cos\phi_{CP}| \gtrsim 0.8$, are excluded at 2σ.

B. Study of the tqH process

The analysis of the tqH process uses the $\mathcal{D}_{0-}$, $\mathcal{D}_{\rm bkg}$, $\mathcal{D}_{\rm bkg}^{\rm int}$ discriminants, shown in Fig. 12. In this study, the $Hf\bar{f}$-induced process is considered as signal, and the HVV-induced process is considered as background. Similar to the $t\bar{t}H$ study, the decay of the top quarks is not considered in the matrix element, and the $\mathcal{D}_{CP}$ discriminants provide little information and therefore are not used. There is a sizable contribution of the $t\bar{t}H$ events misreconstructed as tqH, and they carry information on f_{CP}. The above observables provide sufficient information to differentiate between CP components of the $t\bar{t}H$ process as well.

All event contributions in this study can be parametrized with three couplings, κ, $\tilde{\kappa}$, and a_1, which are assumed to be real, as

$$N_{\rm tot}^{tqH} = \mathcal{L}(a_1^2\sigma_{\rm bkg}^{tqH} + \kappa^2\sigma_{0+}^{tqH} + \tilde{\kappa}^2\sigma_{0-}^{tqH} + a_1\kappa\sigma_{\rm int(bkg,0+)}^{tqH} + a_1\tilde{\kappa}\sigma_{\rm int(bkg,0-)}^{tqH} + \kappa\tilde{\kappa}\sigma_{\rm int(0-,0+)}^{tqH}), \quad (13)$$

$$N_{\rm tot}^{t\bar{t}H} = \mathcal{L}(\kappa^2\sigma_{0+}^{t\bar{t}H} + \tilde{\kappa}^2\sigma_{0-}^{ttH} + \kappa\tilde{\kappa}\sigma_{\rm int(0-,0+)}^{ttH}), \quad (14)$$

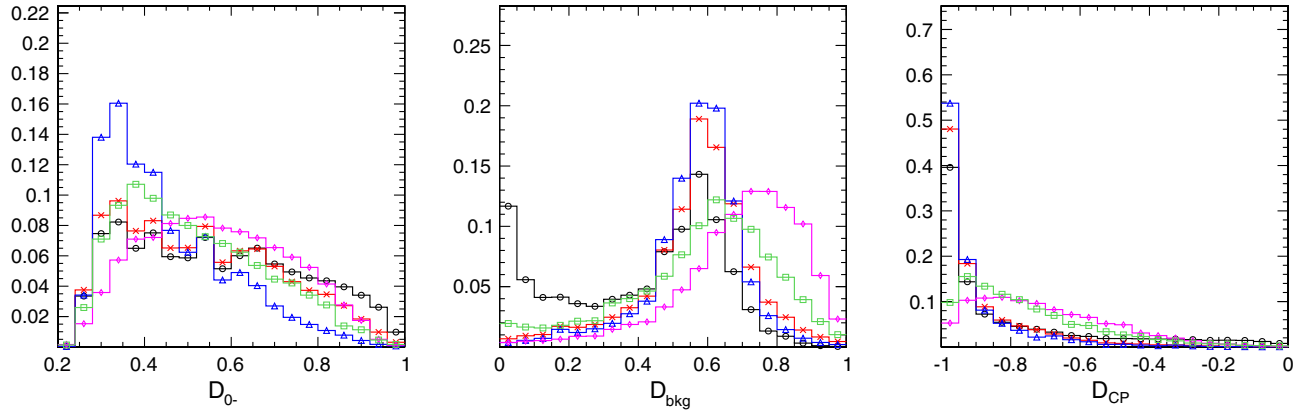

FIG. 12. Distributions of $\mathcal{D}_{0-}$ (left), $\mathcal{D}_{\rm bkg}$ (middle), and $\mathcal{D}^{\rm int}_{\rm bkg}$ (right) discriminants in the tqH study where the $Hf\bar{f}$-induced process is considered as signal and the HVV-induced process is considered as background. The following three contributions are considered: $J^P = 0^+$ signal (red crosses), 0^- signal (blue triangles), and HVV-induced process as background (black circles). Also shown are distributions of misreconstructed $t\bar{t}H$ signal with $J^P = 0^+$ (magenta diamonds) and 0^- signal (green squares). All distributions appear after simulation and reconstruction discussed in the text.

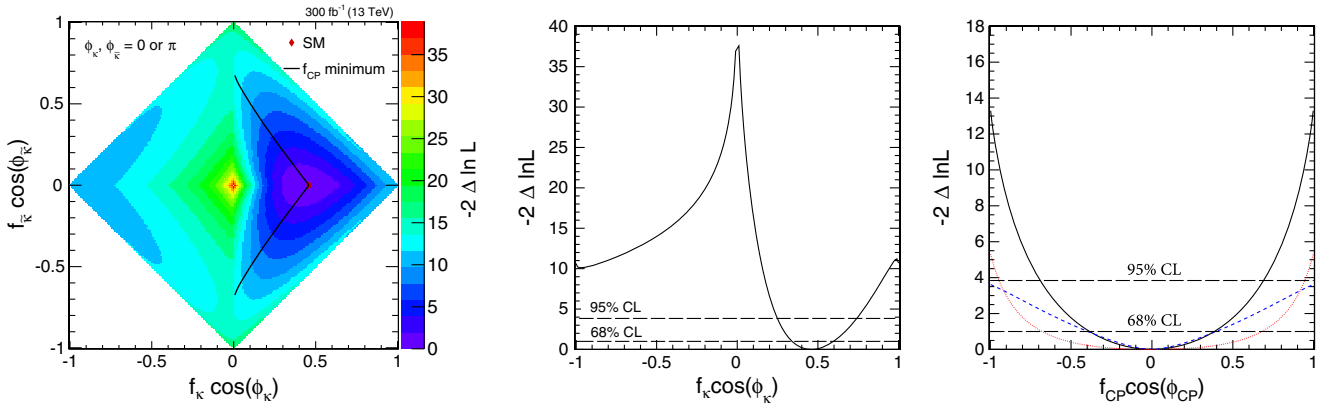

FIG. 13. The likelihood scan of parameters of interest in the tqH study expected with 300 fb^{-1} at LHC. Left: $f_{\tilde{\kappa}}\cos(\phi_{\tilde{\kappa}})$ vs $f_\kappa\cos(\phi_\kappa)$, where the SM expectation is $f_\kappa = 0.46$ and $f_{\tilde{\kappa}} = 0$ and where $\phi_{\tilde{\kappa}}$ or $\phi_{CP} = 0$ or π. Middle: $f_\kappa\cos(\phi_\kappa)$ with the constraint of no anomalous couplings, $f_{\tilde{\kappa}} = 0$. Right: $f_{CP}\cos(\phi_{CP})$ corresponding to the curved line on the left plot going from $f_\kappa = 0$ ($f_{CP} = 1$) to $f_{\tilde{\kappa}} = 0$ ($f_{CP} = 0$) following the minimum of $-2\Delta\ln\mathcal{L}$. The solid line shows the expectation considering all contributions, while the red dotted line assumes that only $t\bar{t}H$ misreconstructed events are present in the sample, and the blue dashed line assumes no contribution of $t\bar{t}H$ events.

where $\mathcal{L}$ is integrated luminosity and σ is the product of cross section and reconstruction efficiency of a particular process corresponding to the unit value of the coupling (κ, $\tilde{\kappa}$, or a_1). The interference cross section can be negative, as it is for interference between the κ and a_1 terms in the tqH process. In the tqH process, we express κ, $\tilde{\kappa}$, and a_1 in terms of two effective cross section fractions with phases and the overall normalization as follows:

$$f_\kappa = \frac{\kappa^2\sigma^{tqH}_{0+}}{(a_1^2\sigma^{tqH}_{\rm bkg} + \kappa^2\sigma^{tqH}_{0+} + \tilde{\kappa}^2\sigma^{tqH}_{0-})},$$
$$\phi_\kappa = \arg(\kappa/a_1) = 0 \text{ or } \pi, \qquad (15)$$

$$f_{\tilde{\kappa}} = \frac{\tilde{\kappa}^2\sigma^{tqH}_{0-}}{(a_1^2\sigma^{tqH}_{\rm bkg} + \kappa^2\sigma^{tqH}_{0+} + \tilde{\kappa}^2\sigma^{tqH}_{0-})},$$
$$\phi_{\tilde{\kappa}} = \arg(\tilde{\kappa}/a_1) = 0 \text{ or } \pi. \qquad (16)$$

In the SM, $f_\kappa = 0.46$, $f_{\tilde{\kappa}} = 0$, and $\phi_\kappa = 0$. The ratios of the cross section is $\sigma^{tqH}_{0+}/\sigma^{tqH}_{\rm bkg} = 0.86$.

The maximum likelihood fit, similar to the $t\bar{t}H$ analysis, uses a 3D template approach of three observables $\mathcal{D}_{0-}$, $\mathcal{D}_{\rm bkg}$, $\mathcal{D}^{\rm int}_{\rm bkg}$, with f_κ, $f_{\tilde{\kappa}}$, and the total event yield as free parameters. The expected precision of the fit is shown in Fig. 13 (left plot). This approach allows simultaneous measurement of both the relative fraction of HVV- and $Hf\bar{f}$-induced processes and of the anomalous contribution

in the $Hf\bar{f}$ coupling, with proper accounting for all interference effects. This measurement can be reduced either to the measurement of f_κ with the constraint $f_{\tilde{\kappa}} = f_{CP} = 0$ (middle plot) or to the measurement of f_{CP} (right plot). Precision on the $Hf\bar{f}$ couplings is driven by both tqH and $t\bar{t}H$ processes in this analysis, as illustrated with the likelihood scans separated for the two samples of events in the right plot of Fig. 13. More than 3σ exclusion of the pure pseudoscalar state is expected in such a scenario, which is a measurement independent from that discussed in Sec. VI A since $t\bar{t}H$ events have little overlap. It is important to note that in this scenario it will be possible to determine the relative sign of the $Hf\bar{f}$- and HVV-induced contributions and exclude both extreme scenarios of either pure $Hf\bar{f}$ or pure HVV processes, assuming events follow SM expectation.

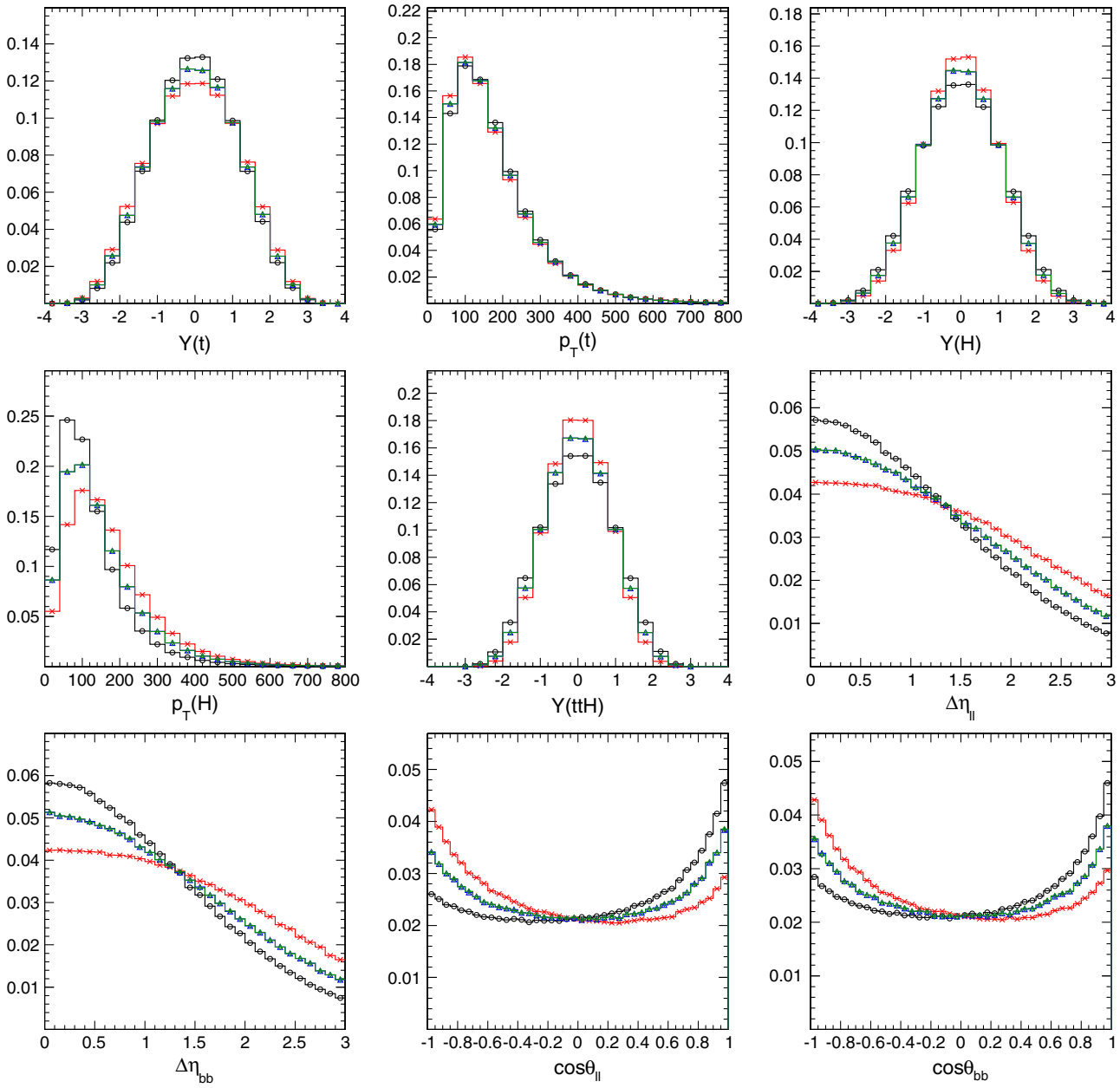

FIG. 14. The kinematic distributions in the process gg and $q\bar{q} \to t\bar{t}H$ defined in the laboratory frame: top-quark rapidity $[Y(t)]$, transverse momentum of the top quark $[p_T(t)]$, H boson rapidity $[Y(t)]$, transverse momentum of the H boson $[p_H(t)]$, $t\bar{t}H$ system rapidity $[Y(t\bar{t}H)]$, pseudorapidity difference between the two down-type fermions decayed from top and antitop $(\Delta\eta_{ll})$ and between two bottom quarks $(\Delta\eta_{bb})$, $\cos\theta_{ll}$ between the two down-type fermions, and $\cos\theta_{bb}$ between the two bottom quarks. Four scenarios of anomalous $t\bar{t}H$ couplings are shown: $f_{CP} = 0$ (SM 0^+, black circles), $f_{CP} = 1$ (pseudoscalar 0^-, red crosses), $f_{CP} = 0.28$ with $\phi_{CP} = 0$ (blue triangles), and $\phi_{CP} = \pi/2$ (green diamonds). The LHC pp energy of 13 TeV and H boson mass of 125 GeV are used in simulation.

VII. SUMMARY AND CONCLUSIONS

We have developed the Monte Carlo simulation and matrix element analysis tools and investigated prospects for the measurement of anomalous interactions in the H boson production in association with top or bottom quarks at the LHC, as well as its decay in two tau leptons. The study is based on the JHU generator framework and the matrix element MELA analysis technique. We find that it is difficult to measure anomalous couplings in the $b\bar{b}H$ process, while in both $t\bar{t}H$ and tqH analyses, it is possible to have more than 3σ separation of the pseudoscalar hypothesis from the scalar with 300 fb^{-1} of integrated luminosity at LHC at 13 TeV. It is also possible to separate the $Hf\bar{f}$ and HVV processes and determine their relative phase in the tqH production, where in the SM the two processes interfere strongly and destructively. This feasibility study considers only representative decay channels of the top quark (hadronic decay of one top) and H boson (diboson decay), and inclusion of other final states would only enhance expected precision. Systematic uncertainties from QCD effects, such as PDF, scale, parton showering, and higher-order corrections, are shown to be relatively small compared to expected statistical precision. The tools and techniques presented should facilitate measurements of SM and anomalous $Hf\bar{f}$ couplings.

ACKNOWLEDGMENTS

We acknowledge contribution of CMS Collaboration colleagues to the MELA project development and thank Roberto Covarelli, Chris Martin, and Candice You for help with the generator validation. We are grateful to our coauthors of the JHU generator project for valuable contributions and in particular to Ulascan Sarica and Heshy Roskes for the generator package support and Fabrizio Caola for providing useful comments on the manuscript. This research is partially supported by U.S. NSF under Grant No. PHY-1404302 and by the German Federal Ministry for Education and Research (BMBF) under Grant No. 05H15VKCCA. Calculations reported in this paper were performed on the Homewood High Performance Cluster of the Johns Hopkins University and the Maryland Advanced Research Computing Center.

APPENDIX: SUPPLEMENTAL INFORMATION ON KINEMATICS

Figure 14 shows the kinematic observables defined in the laboratory frame in the SM process gg and $q\bar{q} \to t\bar{t}H$, corresponding to four scenarios of anomalous $t\bar{t}H$ couplings. These observables can be derived from those shown in Fig. 5 and defined in Sec. IV A.

[1] ATLAS Collaboration, Observation of a new particle in the search for the Standard Model Higgs boson with the ATLAS detector at the LHC, Phys. Lett. B **716**, 1 (2012).
[2] CMS Collaboration, Observation of a new boson at a mass of 125 GeV with the CMS experiment at the LHC, Phys. Lett. B **716**, 30 (2012).
[3] CMS Collaboration, Constraints on the spin-parity and anomalous HVV couplings of the Higgs boson in proton collisions at 7 and 8 TeV, Phys. Rev. D **92**, 012004 (2015).
[4] CMS Collaboration, Precise determination of the mass of the Higgs boson and tests of compatibility of its couplings with the standard model predictions using proton collisions at 7 and 8 TeV, Eur. Phys. J. C **75**, 212 (2015).
[5] ATLAS Collaboration, Study of the spin and parity of the Higgs boson in diboson decays with the ATLAS detector, Eur. Phys. J. C **75**, 476 (2015).
[6] ATLAS Collaboration, Measurements of the Higgs boson production and decay rates and coupling strengths using pp collision data at $\sqrt{s} = 7$ and 8 TeV in the ATLAS experiment, Eur. Phys. J. C **76**, 6 (2016).
[7] S. Dawson *et al.*, Higgs Working Group Report of the Snowmass 2013 Community Planning Study, arXiv:1310.8361.
[8] P. S. Bhupal Dev, A. Djouadi, R. M. Godbole, M. M. Mühlleitner, and S. D. Rindani, Determining the CP properties of the Higgs boson, Phys. Rev. Lett. **100**, 051801 (2008).
[9] P. Agrawal, S. Mitra, and A. Shivaji, Effect of anomalous couplings on the associated production of a single top quark and a Higgs boson at the LHC, J. High Energy Phys. 12 (2013) 077.
[10] M. Farina, C. Grojean, F. Maltoni, E. Salvioni, and A. Thamm, Lifting degeneracies in Higgs couplings using single top production in association with a Higgs boson, J. High Energy Phys. 05 (2013) 022.
[11] K. Nishiwaki, S. Niyogi, and A. Shivaji, ttH anomalous coupling in double Higgs production, J. High Energy Phys. 04 (2014) 011.
[12] S. Biswas, E. Gabrielli, F. Margaroli, and B. Mele, Direct constraints on the top-Higgs coupling from the 8 TeV LHC data, J. High Energy Phys. 07 (2013) 073.
[13] J. Ellis, D. S. Hwang, K. Sakurai, and M. Takeuchi, Disentangling Higgs-top couplings in associated production, J. High Energy Phys. 04 (2014) 004.
[14] S. Khatibi and M. M. Najafabadi, Exploring the anomalous Higgs-top couplings, Phys. Rev. D **90**, 074014 (2014).
[15] L. Wu, Enhancing thj production from top-Higgs FCNC couplings, J. High Energy Phys. 02 (2015) 061.

[16] F. Demartin, F. Maltoni, K. Mawatari, B. Page, and M. Zaro, Higgs characterisation at NLO in QCD: *CP* properties of the top-quark Yukawa interaction, Eur. Phys. J. C **74**, 3065 (2014).
[17] J. Bramante, A. Delgado, and A. Martin, Cornering a hyper Higgs boson: Angular kinematics for boosted Higgs bosons with top pairs, Phys. Rev. D **89**, 093006 (2014).
[18] A. Kobakhidze, L. Wu, and J. Yue, Anomalous top-Higgs couplings and top polarisation in single top and Higgs associated production at the LHC, J. High Energy Phys. 10 (2014) 100.
[19] C. Englert and E. Re, Bounding the top Yukawa coupling with Higgs-associated single-top production, Phys. Rev. D **89**, 073020 (2014).
[20] J. Chang, K. Cheung, J. S. Lee, and C.-T. Lu, Probing the top-Yukawa coupling in associated Higgs production with a single top quark, J. High Energy Phys. 05 (2014) 062.
[21] J. Yue, Enhanced thj signal at the LHC with $h \to \gamma\gamma$ decay and *CP*-violating top-Higgs coupling, Phys. Lett. B **744**, 131 (2015).
[22] X.-G. He, G.-N. Li, and Y.-J. Zheng, Probing Higgs boson *CP* Properties with $t\bar{t}H$ at the LHC and the 100 TeV pp collider, Int. J. Mod. Phys. A **30**, 1550156 (2015).
[23] F. Boudjema, R. M. Godbole, D. Guadagnoli, and K. A. Mohan, Laboratory-frame observables for probing the top-Higgs boson interaction, Phys. Rev. D **92**, 015019 (2015).
[24] K. Kolodziej and A. Slapik, Probing the top-Higgs coupling through the secondary lepton distributions in the associated production of the top-quark pair and Higgs boson at the LHC, Eur. Phys. J. C **75**, 475 (2015).
[25] Y. Chen, D. Stolarski, and R. Vega-Morales, Golden probe of the top Yukuwa coupling, Phys. Rev. D **92**, 053003 (2015).
[26] F. Demartin, F. Maltoni, K. Mawatari, and M. Zaro, Higgs production in association with a single top quark at the LHC, Eur. Phys. J. C **75**, 267 (2015).
[27] M. R. Buckley and D. Goncalves, Boosting the Direct *CP* Measurement of the Higgs-Top Coupling, Phys. Rev. Lett. **116**, 091801 (2016).
[28] N. Mileo, K. Kiers, A. Szynkman, D. Crane, and E. Gegner, Pseudoscalar top-Higgs coupling: Exploration of *CP*-odd observables to resolve the sign ambiguity, J. High Energy Phys. 07 (2016) 056.
[29] S. D. Rindani, P. Sharma, and A. Shivaji, Unraveling the CP phase of top-Higgs coupling in associated production at the LHC, Phys. Lett. B **761**, 25 (2016).
[30] V. Cirigliano, W. Dekens, J. de Vries, and E. Mereghetti, Constraining the top-Higgs sector of the standard model effective field theory, Phys. Rev. D **94**, 034031 (2016).
[31] M. J. Dolan, M. Spannowsky, Q. Wang, and Z.-H. Yu, Determining the quantum numbers of simplified models in $t\bar{t}X$ production at the LHC, Phys. Rev. D **94**, 015025 (2016).
[32] K. Desch, A. Imhof, Z. Was, and M. Worek, Probing the *CP* nature of the Higgs boson at linear colliders with tau spin correlations: The Case of mixed scalar—pseudoscalar couplings, Phys. Lett. B **579**, 157 (2004).
[33] S. Berge, W. Bernreuther, and H. Spiesberger, Determination of the CP parity of Higgs bosons in their tau decay channels at the ILC, arXiv:1208.1507.
[34] R. Harnik, A. Martin, T. Okui, R. Primulando, and F. Yu, Measuring *CP* violation in $h \to \tau^+\tau^-$ at colliders, Phys. Rev. D **88**, 076009 (2013).
[35] S. Berge, W. Bernreuther, and H. Spiesberger, Higgs *CP* properties using the τ decay modes at the ILC, Phys. Lett. B **727**, 488 (2013).
[36] P. Ilten, Electroweak and Higgs measurements using tau final states with the LHCb detector, arXiv:1401.4902.
[37] S. Berge, W. Bernreuther, and S. Kirchner, Prospects of constraining the Higgs bosons *CP* nature in the tau decay channel at the LHC, Phys. Rev. D **92**, 096012 (2015).
[38] A. Askew, P. Jaiswal, T. Okui, H. B. Prosper, and N. Sato, Prospect for measuring the *CP* phase in the $h\tau\tau$ coupling at the LHC, Phys. Rev. D **91**, 075014 (2015).
[39] CMS Collaboration, Search for the associated production of a Higgs boson with a single top quark in proton-proton collisions at $\sqrt{s} = 8$ TeV, J. High Energy Phys. 06 (2016) 177.
[40] CMS Collaboration, Search for the associated production of the Higgs boson with a top-quark pair, J. High Energy Phys. 09 (2014) 087 [J. High Energy Phys. 10 (2014) 106(E).
[41] CMS Collaboration, Search for a Standard Model Higgs boson produced in association with a top-quark pair and decaying to bottom quarks using a matrix element method, Eur. Phys. J. C **75**, 251 (2015).
[42] ATLAS Collaboration, Search for the associated production of the Higgs boson with a top quark pair in multilepton final states with the ATLAS detector, Phys. Lett. B **749**, 519 (2015).
[43] ATLAS Collaboration, Search for the Standard Model Higgs boson decaying into $b\bar{b}$ produced in association with top quarks decaying hadronically in pp collisions at $\sqrt{s} = 8$ TeV with the ATLAS detector, J. High Energy Phys. 05 (2016) 160.
[44] CMS Collaboration, Search for the standard model Higgs boson produced in association with a W or a Z boson and decaying to bottom quarks, Phys. Rev. D **89**, 012003 (2014).
[45] ATLAS Collaboration, Search for the $b\bar{b}$ decay of the Standard Model Higgs boson in associated $(W/Z)H$ production with the ATLAS detector, J. High Energy Phys. 01 (2015) 069.
[46] CMS Collaboration, Search for the standard model Higgs boson produced through vector boson fusion and decaying to $b\bar{b}$, Phys. Rev. D **92**, 032008 (2015).
[47] CMS Collaboration, Evidence for the 125 GeV Higgs boson decaying to a pair of τ leptons, J. High Energy Phys. 05 (2014) 104.
[48] ATLAS Collaboration, Evidence for the Higgs-boson Yukawa coupling to tau leptons with the ATLAS detector, J. High Energy Phys. 04 (2015) 117.
[49] ATLAS Collaboration, Search for lepton-flavour-violating $H \to \mu\tau$ decays of the Higgs boson with the ATLAS detector, J. High Energy Phys. 11 (2015) 211.

[50] CMS Collaboration, Search for a very light NMSSM Higgs boson produced in decays of the 125 GeV scalar boson and decaying into τ leptons in pp collisions at $\sqrt{s} = 8$ TeV, J. High Energy Phys. 01 (2016) 079.
[51] CMS Collaboration, Search for a low-mass pseudoscalar Higgs boson produced in association with a b-bbar pair in pp collisions at sqrt$(s) = 8$ TeV, Phys. Lett. B **758**, 296 (2016).
[52] CMS Collaboration, Study of the Mass and Spin-Parity of the Higgs Boson Candidate Via Its Decays to Z Boson Pairs, Phys. Rev. Lett. **110**, 081803 (2013).
[53] CMS Collaboration, Measurement of the properties of a Higgs boson in the four-lepton final state, Phys. Rev. D **89**, 092007 (2014).
[54] CMS Collaboration, Measurement of Higgs boson production and properties in the WW decay channel with leptonic final states, J. High Energy Phys. 01 (2014) 096.
[55] CMS Collaboration, Constraints on the Higgs boson width from off-shell production and decay to Z-boson pairs, Phys. Lett. B **736**, 64 (2014).
[56] CMS Collaboration, Observation of the diphoton decay of the Higgs boson and measurement of its properties, Eur. Phys. J. C **74**, 3076 (2014).
[57] CMS Collaboration, Limits on the Higgs boson lifetime and width from its decay to four charged leptons, Phys. Rev. D **92**, 072010 (2015).
[58] CMS Collaboration, Combined search for anomalous pseudoscalar HVV couplings in VH production and H to VV decay, Phys. Lett. B **759**, 672 (2016).
[59] ATLAS Collaboration, Evidence for the spin-0 nature of the Higgs boson using ATLAS data, Phys. Lett. B **726**, 120 (2013).
[60] ATLAS Collaboration, Test of CP invariance in vector-boson fusion production of the Higgs boson using the optimal observable method in the ditau decay channel with the ATLAS detector, arXiv:1602.04516.
[61] Y. Gao, A. V. Gritsan, Z. Guo, K. Melnikov, M. Schulze, and N. V. Tran, Spin determination of single-produced resonances at hadron colliders, Phys. Rev. D **81**, 075022 (2010).
[62] S. Bolognesi, Y. Gao, A. V. Gritsan, K. Melnikov, M. Schulze, N. V. Tran, and A. Whitbeck, Spin and parity of a single-produced resonance at the LHC, Phys. Rev. D **86**, 095031 (2012).
[63] I. Anderson *et al.*, Constraining anomalous HVV interactions at proton and lepton colliders, Phys. Rev. D **89**, 035007 (2014).
[64] J. R. Andersen, C. Englert, and M. Spannowsky, Extracting precise Higgs couplings by using the matrix element method, Phys. Rev. D **87**, 015019 (2013).
[65] P. Artoisenet, P. de Aquino, F. Maltoni, and O. Mattelaer, Unravelling $t\bar{t}h$ via the Matrix Element Method, Phys. Rev. Lett. **111**, 091802 (2013).
[66] G. Bevilacqua, H. B. Hartanto, M. Kraus, and M. Worek, Top Quark Pair Production in Association with a Jet with Next-to-Leading-Order QCD Off-Shell Effects at the Large Hadron Collider, Phys. Rev. Lett. **116**, 052003 (2016).
[67] R. Rontsch and M. Schulze, Constraining couplings of top quarks to the Z boson in $t\bar{t} + Z$ production at the LHC, J. High Energy Phys. 07 (2014) 091.
[68] R. Rontsch and M. Schulze, Probing top-Z dipole moments at the LHC and ILC, J. High Energy Phys. 08 (2015) 044.
[69] G. Ossola, C. G. Papadopoulos, and R. Pittau, Reducing full one-loop amplitudes to scalar integrals at the integrand level, Nucl. Phys. **B763**, 147 (2007).
[70] R. K. Ellis, W. T. Giele, and Z. Kunszt, A Numerical Unitarity Formalism for Evaluating One-Loop Amplitudes, J. High Energy Phys. 03 (2008) 003.
[71] W. T. Giele, Z. Kunszt, and K. Melnikov, Full one-loop amplitudes from tree amplitudes, J. High Energy Phys. 04 (2008) 049.
[72] R. K. Ellis, W. T. Giele, Z. Kunszt, and K. Melnikov, Masses, fermions and generalized D-dimensional unitarity, Nucl. Phys. **B822**, 270 (2009).
[73] S. Catani and M. H. Seymour, A General algorithm for calculating jet cross-sections in NLO QCD, Nucl. Phys. **B485**, 291 (1997) [**B510**, 503(E) (1998)].
[74] S. Catani, S. Dittmaier, M. H. Seymour, and Z. Trocsanyi, The Dipole formalism for next-to-leading order QCD calculations with massive partons, Nucl. Phys. **B627**, 189 (2002).
[75] K. Melnikov and M. Schulze, NLO QCD corrections to top quark pair production and decay at hadron colliders, J. High Energy Phys. 08 (2009) 049.
[76] A. Denner, R. Feger, and A. Scharf, Irreducible background and interference effects for Higgs-boson production in association with a top-quark pair, J. High Energy Phys. 04 (2015) 008.
[77] A. Denner and R. Feger, NLO QCD corrections to off-shell top-antitop production with leptonic decays in association with a Higgs boson at the LHC, J. High Energy Phys. 11 (2015) 209.
[78] J. Campbell, R. K. Ellis, and R. Rontsch, Single top production in association with a Z boson at the LHC, Phys. Rev. D **87**, 114006 (2013).
[79] F. Maltoni, K. Paul, T. Stelzer, and S. Willenbrock, Associated production of Higgs and single top at hadron colliders, Phys. Rev. D **64**, 094023 (2001).
[80] S. Jadach, J. H. Kuhn, and Z. Wąs, TAUOLA—a library of Monte Carlo programs to simulate decays of polarized tau leptons, Comput. Phys. Commun. **64**, 275 (1991).
[81] T. Sjöstrand, S. Mrenna, and P. Skands, PYTHIA 6.4 physics and manual, J. High Energy Phys. 05 (2006) 026.
[82] T. Sjöstrand, S. Mrenna, and P. Z. Skands, A Brief Introduction to PYTHIA 8.1, Comput. Phys. Commun. **178**, 852 (2008).
[83] J. Alwall *et al.*, A Les Houches interface for BSM generators, arXiv:0712.3311.
[84] S. Frixione, P. Nason, and C. Oleari, Matching NLO QCD computations with Parton Shower simulations: the POWHEG method, J. High Energy Phys. 11 (2007) 070.
[85] H. B. Hartanto, B. Jager, L. Reina, and D. Wackeroth, Higgs boson production in association with top quarks in the POWHEG BOX, Phys. Rev. D **91**, 094003 (2015).
[86] B. Jager, L. Reina, and D. Wackeroth, Higgs boson production in association with b jets in the POWHEG BOX, Phys. Rev. D **93**, 014030 (2016).

[87] R. Frederix, S. Frixione, V. Hirschi, F. Maltoni, R. Pittau, and P. Torrielli, Scalar and pseudoscalar Higgs production in association with a top-antitop pair, Phys. Lett. B **701**, 427 (2011).
[88] J. Alwall, R. Frederix, S. Frixione, V. Hirschi, F. Maltoni, O. Mattelaer, H.-S. Shao, T. Stelzer, P. Torrielli, and M. Zaro, The automated computation of tree-level and next-to-leading order differential cross sections, and their matching to parton shower simulations, J. High Energy Phys. 07 (2014) 079.
[89] NNPDF Collaboration, Parton distributions for the LHC Run II, J. High Energy Phys. 04 (2015) 040.
[90] S. Heinemeyer *et al.* (LHC Higgs Cross Section Working Group), Handbook of LHC Higgs Cross Sections: 3. Higgs Properties, arXiv:1307.1347.
[91] CMS Collaboration, Search for a Higgs Boson in the Mass Range from 145 to 1000 GeV Decaying to a Pair of W or Z Bosons, J. High Energy Phys. 10 (2015) 144.
[92] K. Cranmer, J. Pavez, and G. Louppe, Approximating likelihood ratios with calibrated discriminative classifiers, arXiv:1506.02169.
[93] J. Neyman and E. S. Pearson, On the Problem of the Most Efficient Tests of Statistical Hypotheses, Phil. Trans. R. Soc. A **231**, 289 (1933).
[94] D. Atwood and A. Soni, Analysis for magnetic moment and electric dipole moment form-factors of the top quark via $e^+e^- \to t\bar{t}$, Phys. Rev. D **45**, 2405 (1992).
[95] M. Davier, L. Duflot, F. Le Diberder, and A. Rouge, The optimal method for the measurement of tau polarization, Phys. Lett. B **306**, 411 (1993).
[96] M. Diehl and O. Nachtmann, Optimal observables for the measurement of three gauge boson couplings in $e^+e^- \to W^+W^-$, Z. Phys. C **62**, 397 (1994).
[97] J. Alwall, A. Freitas, and O. Mattelaer, The matrix element method and QCD radiation, Phys. Rev. D **83**, 074010 (2011).
[98] J. M. Campbell, W. T. Giele, and C. Williams, The matrix element method at next-to-leading order, J. High Energy Phys. 11 (2012) 043.
[99] J. M. Campbell, R. K. Ellis, W. T. Giele, and C. Williams, Finding the Higgs boson in decays to $Z\gamma$ using the matrix element method at Next-to-Leading Order, Phys. Rev. D **87**, 073005 (2013).
[100] T. Martini and P. Uwer, Extending the Matrix Element Method beyond the Born approximation: Calculating event weights at next-to-leading order accuracy, J. High Energy Phys. 09 (2015) 083.
[101] D. E. Soper and M. Spannowsky, Finding physics signals with event deconstruction, Phys. Rev. D **89**, 094005 (2014).
[102] D. E. Soper and M. Spannowsky, Finding physics signals with shower deconstruction, Phys. Rev. D **84**, 074002 (2011).
[103] C. Englert, O. Mattelaer, and M. Spannowsky, Measuring the Higgs-bottom coupling in weak boson fusion, Phys. Lett. B **756**, 103 (2016).
[104] N. Eminizer and M. Swartz (private communications).